Copyright

by

Rachel Melanie Anderson

2015

The Dissertation Committee for Rachel Melanie Anderson
Certifies that this is the approved version of the
following dissertation:

Dendrimer-Encapsulated Nanoparticles as Model Electrocatalysts

Committee:

Richard M. Crooks, Supervisor

Graeme Henkelman

Keith J. Stevenson

Simon M. Humphrey

Charles Buddie Mullins

Dendrimer-Encapsulated Nanoparticles as Model Electrocatalysts

by

Rachel Melanie Anderson, B.S.

Dissertation

Presented to the Faculty of the Graduate School of

The University of Texas at Austin

in Partial Fulfillment

of the Requirements

for the Degree of

Doctor of Philosophy

The University of Texas at Austin

December, 2015

Acknowledgements

I would first like to acknowledge my advisor, Dr. Richard Crooks, for the guidance and the many opportunities he has provided me throughout my graduate career. I would also like to thank Drs. Graeme Henkelman, Keith Stevenson, Simon Humphrey, and Buddie Mullins for serving on my committee and for their feedback and collaborations, as well as Drs. Anatoly Frenkel and Stanko Brankovic for all that I have learned from them in their respective areas of expertise. My undergraduate research advisor, Dr. Samuel Kounaves, introduced me to scientific research and helped me progress towards my goal of graduate school.

My research group has always played an important part in problem solving in the lab, but also made the time spent there more enjoyable. I would like to acknowledge Susie Myers and Emily Carino for helping me get started, and thank in particular David Yancey and Morgan Anderson. The collaboration with the Henkelman group has yielded many interesting discussions and joint projects, and I'd especially like to thank my colleagues Liang Zhang and Samuel Chill. Angie Missildine and Betsy Hamblen have also been very helpful along the way.

I'd like to thank my friends and family for their support. First, my classmates Nellymar Membreño, Karen Scida,

Netz Arroyo, and Stephany Garcia, not only was I lucky enough to find great study partners and collaborators in my first year, but lifelong friends as well! Mauro Mugnai has been my daily support system and reminder that science can be truly enjoyable. My sister, Gwendolyn, who warned me this would be difficult and then talked me through it anyway. She is the reason I first went into science and her guidance has always meant a lot to me. Most importantly, I'd like to thank my parents, who have always been incredibly supportive and encouraging.

Dendrimer-Encapsulated Nanoparticles as Model Electrocatalysts

Rachel Melanie Anderson, Ph.D.

The University of Texas at Austin, 2015

Supervisor: Richard M. Crooks

In this dissertation, dendrimer-encapsulated nanoparticles (DENs) are employed as model electrocatalysts. DENs are well-defined nanoparticles in the 1-2 nm size range. Nanoparticles consisting of 55-225 atoms are large enough to be synthesized and adequately characterized, but small enough to be modeled theoretically by density functional theory (DFT). In this size range, large deviations from bulk structural characteristics are observed. Characterization and electrocatalytic testing is performed for comparison to theoretical calculations. In this way we are able to better understand nanoparticle structure, as well as validate theoretical models.

A solution based synthesis is used to produce Pd@Pt core@shell DENs, which has been theoretically predicted to have improved activity for the oxygen reduction reaction (ORR). However, through in situ extended X-ray absorption

fine structure (EXAFS) spectroscopy characterization it is determined that structural inversion occurs in which the more noble Pt partitions to the core and the shell becomes enriched in Pd. Larger Pd@Pt nanoparticles (>3 nm) are known to retain their core@shell structure, but 1-2 nm nanoparticles tend to be structurally unstable. Therefore we infer that the observations reported here are driven by the energetics of the small number of atoms present in particles having sizes of <2 nm.

A synthetic strategy for improved fully reduced Pt DENs is also outlined. DENs produced by galvanic exchange of Pt^{2+} salt for Cu DENs overcome the previous limitation of partial Pt reduction when a chemical reducing agent is used. Pt DENs by galvanic exchange are fully reduced and are an improved model electrocatalyst. These galvanic exchange Pt DENs are then studied by in situ electrochemical infrared spectroscopy to probe the stretching frequency of adsorbed CO. These studies show a redshift in the frequency of adsorbed CO, in relation to a Pt(111) single crystal surface, revealing stronger binding of CO to the Pt DENs surface. This shift is confirmed by theoretical calculations. This system is a good future platform to test predictions of the CO binding energy trends on DENs, and to test its use as a descriptor for more complex electrocatalytic reactions.

Table of Contents

List of Tables

List of Figures

List of Illustrations

Chapter 1: Introduction*

The Role of model electrocatalysts

An emerging strategy for discovering the next generation of catalysts involves utilizing high-level computational methods to predict and screen structure/function relationships. This is due in large part to rapidly advancing computational speed and accessibility. However, a key element in the computational paradigm is the need for well-defined experimental models against which theoretical approaches can be validated. The aim is to connect theoretical and experimental methods into an integrated research program. If this connection can be made sufficiently robust and efficient, then we envision that catalyst discovery and optimization will be accelerated significantly.

Experimental control of catalyst structure is a prerequisite for effective comparison of theory and experiment. The simplest model system is a perfect, infinite single crystal, and materials approaching this ideal have been profitably studied for many years.[1-6] Usually, however,

* Anderson, R. M.; Yancey, D. F.; Zhang, L.; Chill, S. T.; Henkelman, G.; Crooks, R. M. *Acc. Chem. Res.* 2015, *48*, 1351-1357.
All authors aided in the compilation and writing of this review article.

nanoparticle models are more closely related to real catalytic systems, and hence there has been much emphasis in recent years on developing a better understanding of their properties. One approach to this problem has been to focus on nanoparticles having facets that are sufficiently large that their catalytic properties approximate bulk, single-crystal surfaces.[7] Indeed, this is the basis for the extensive interest in shape-controlled nanoparticles, where the facets generally dominate catalytic behavior.[8]

As the size of a nanoparticle decreases, however, edge and corner atoms begin to contribute to its catalytic properties and deviations from bulk behavior are observed. This type of behavior is apparent for metal particles having size of <3 nm, but the most interesting size range is from ~1-2 nm. There are two reasons for this. First, very slight changes to the structure or composition of particles in this size range, or the addition or deletion of a few atoms, can have a dramatic effect on catalysis. Second, particles that contain 30-300 atoms are large enough to effectively characterize but small enough to be analyzed in their entirety using first-principles theory. Of course, there are also problems. For example, such small particles are often unstable and even if they are stable, their native structure may be altered during catalytic reactions. This means that

experimental characterization is difficult and best carried out in situ. Additionally, direct comparison of theory and experiment implies that all nanoparticles in an ensemble are uniform, and this ideal situation can only be approximated, to a greater or lesser extent, at the present time.

One established approach for predicting catalyst activity is through the use of a single thermodynamic descriptor, which acts as a proxy for reaction rate. For example, in the case of the oxygen reduction reaction (ORR) a complex multistep reaction can be represented by the binding energy of atomic oxygen on a metal surface.[9] Within this formalism, there is an ideal binding energy that balances the energy of dissociative adsorption of molecular oxygen and desorption of products. The best candidates are found to have an intermediate oxygen binding energy which results in a "volcano"-shaped trend of activity versus binding energy,[10] as demonstrated in Figure 1.1.

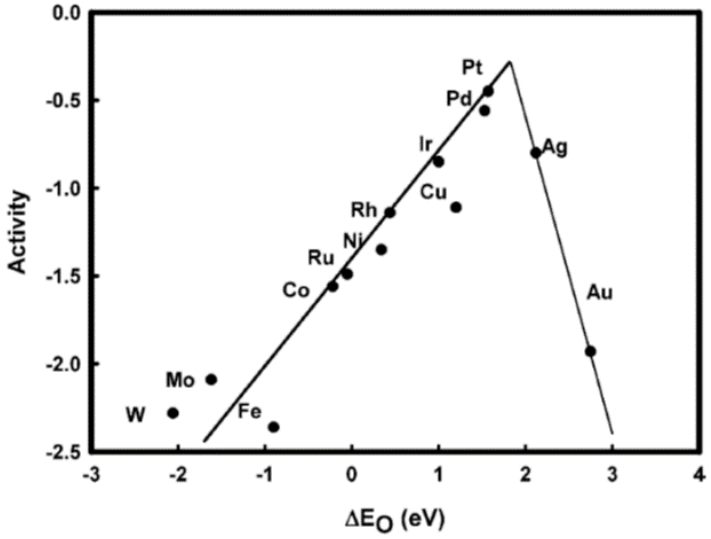

Figure 1.1

Trends in oxygen reduction activity plotted as a function of the oxygen binding energy. *J. Phys. Chem. B* 2004, *108*, 17886-17892. Copyright 2004 American Chemical Society.

This same general strategy has been employed for reactions such as water oxidation[11,12] (OH binding energy), methanol oxidation[13] (CO and OH binding energies), and hydrogen evolution[14] (H binding energy). On a bulk surface this treatment is relatively simple because of the uniformity of the surface structure, but the same approach can be applied to nanoparticles on which a greater variety of binding sites are present. Of the many unique sites on nanoparticles, the most catalytically active can be determined by calculating and comparing the binding energies of the model reaction intermediate or product on each distinctive surface location.

As alluded to earlier, a principal difficulty inherent to correlating experimental catalytic measurements to theory is the polydisperse nature of nanoparticles. There are only three possible solutions to this problem: (1) develop synthetic methods that result in uniform distributions of particle size, composition, and structure; (2) develop theory and calculations that are able to take into account polydispersity; (3) develop methods for carrying out catalytic measurements on just one, or perhaps a few, well-defined nanoparticles. There are significant problems associated with all of these approaches, but some progress has been made. For example, mass-selected particle syntheses result in very good mass uniformity.[15] Likewise, a few studies have been reported involving catalytic measurements on single particles, but the particles are typically rather large and it has not been possible to correlate catalytic rates with nanoparticle structure.[16,17] In addition to the problem of polydispersity, there is another difficulty associated with understanding the catalytic properties of 1-2 nm particles: some kind of capping ligand is required to control growth and minimize agglomeration. Such ligands affect nanoparticle electronic properties, reactant access to surface atoms, and in many cases composition and structure as well.

In this work, dendrimer-encapsulated nanoparticles (DENs)[18-22] are applied as the model electrocatalysts. DENs are nearly monodisperse nanoparticles with tunable sizes (from just a few atoms[23,24] to ~300 atoms) and compositions.[20-22] DENs in the size range of ~0.8 nm to ~2.2 nm are large enough to be characterized experimentally and tested for their catalytic properties, but also small enough to be modeled by ab-initio density functional theory (DFT) calculations. The results of nanoparticle characterization and catalytic testing can then be incorporated into the development of more accurate models for the theoretical prediction of nanoparticle structure and activity. This iterative process, summarized by Illustration 1.1, leads to refinement of the theory and the prediction of better nanoparticle electrocatalyst candidates. This in turn leads to the next generation of more active electrocatalysts that can be used for a wide variety of applications.

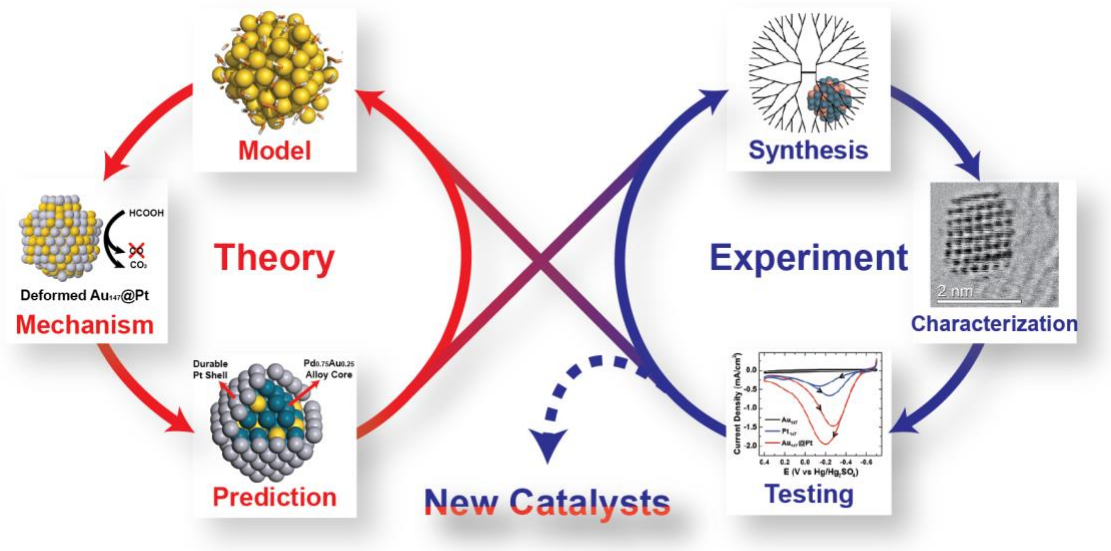

Illustration 1.1

The process for rational catalyst design.

DENDRIMER-ENCAPSULATED NANOPARTICLES

DENs begin to provide a solution to some of the problems mentioned in the previous section. Poly(amidoamine) (PAMAM) dendrimers are branched polymers, which at higher generations form globular structures. The structure of a generation 1 PAMAM dendrimer is shown in Figure 1.2. In this dissertation generation 6 dendrimers are used, which contain 256 tertiary amine groups, 254 terminal groups, have a molecular weight of ~58 kDa, and an estimated diameter of 6.7 nm.[20] At each

branching point, a tertiary amine group is present. These tertiary amine groups are capable of complexing certain metal ions and therefore sequestering them in the interior of the dendrimer. The terminal groups of the dendrimer give them their solubility. In the work presented here, the terminal groups are hydroxyl groups for use in aqueous solutions.

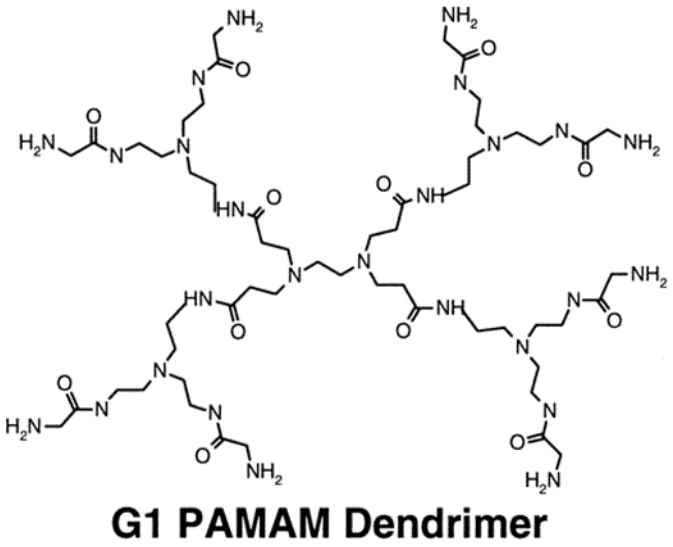

Figure 1.2

Structure of a generation 1 PAMAM dendrimer. *J. Phys. Chem. B* 2005, *109*, 692-704. Copyright 2005 American Chemical Society.

As shown in Illustration 1.2, DENs are synthesized using a two-step templating method. First, metal ions are complexed to the interior of the PAMAM dendrimers. Second, a reducing

agent is added which results in formation of a zerovalent metal nanoparticle that is sterically trapped within the dendrimer interior. This method leads to nanoparticles having an average size controlled by the metal-ion-to-dendrimer ratio present in the precursor solution.

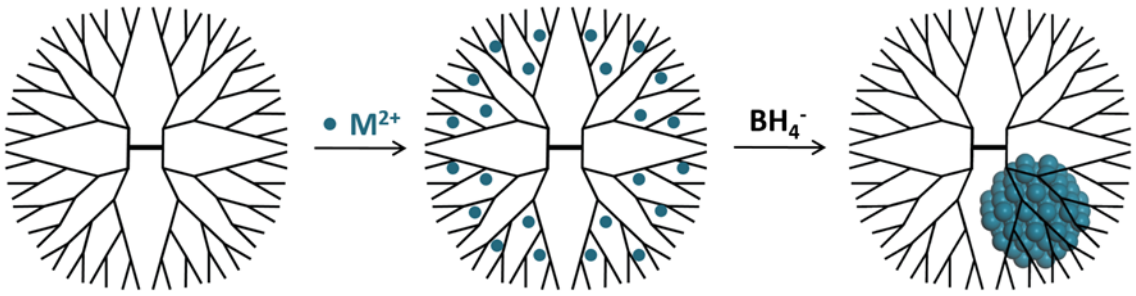

Illustration 1.2

Synthetic Scheme of DENs.

A representative aberration-corrected scanning transmission electron microscopy (ac-STEM) image of a Pt_{147} DEN prepared within a sixth-generation, hydroxyl-terminated PAMAM dendrimer (G6-OH) is shown in Figure 1.3, along with a typical size-distribution histogram. In addition to its templating function, a second important aspect of the dendrimer is that it provides a scaffold for immobilization of DENs on surfaces, such as electrodes,[25] and also prevents direct contact between the surface and the encapsulated nanoparticles. The latter point is important when comparing

experimental and theoretical findings, because support interactions introduce an additional level of complexity.

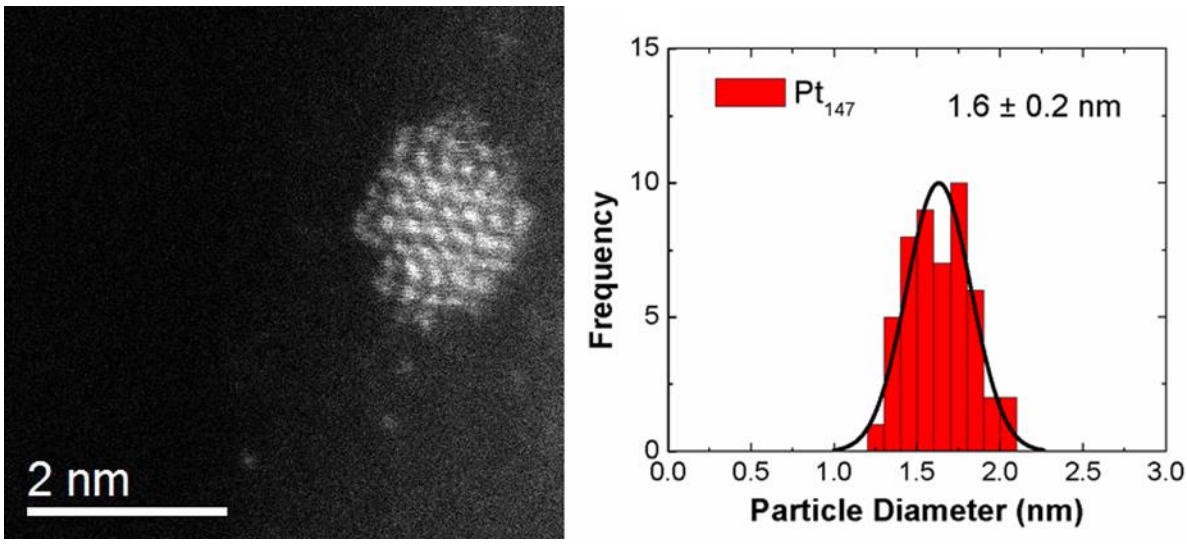

Figure 1.3

Representative ac-STEM image of a Pt_{147} DEN and corresponding size-distribution histogram.

Analytical Methods

While the small size of DENs is an advantage for applying ab-initio DFT calculations, it introduces the challenge of precisely characterizing nanoparticle structure. Common nanoparticle characterization techniques, such as X-ray diffraction (XRD), are more difficult to use and interpret than for nanoparticles just 1 nm larger. For example, XRD analysis requires a synchrotron source and analysis by pair distribution function (PDF).[26,27] Normal high-resolution

transmission electron microscopy (TEM) is helpful, but ac-STEM yields far better resolution which is important for 1-2 nm particles.

More routine analytical methods also provide important information about DENs. For example, UV-vis spectroscopy is a good probe of specific interactions between metal ions and functional groups within the dendrimer (i.e., the DEN precursor), and it also provides some useful information about the DENs themselves. The interaction between the interior tertiary amine groups and the metal ion is seen as a ligand-to-metal charge transfer (LMCT) band. In Figure 1.4 this LMCT is observed in the Cu^{2+}-dendrimer complex at ~300 nm. Once a reducing agent is added (BH_4^-), the LMCT disappears, indicating the formation of zerovalent Cu nanoparticles. This is seen as broadband absorbance increasing towards lower wavelengths. This interaction is sensitive to the oxidation state of the metal ion and the pH of the solution, making this a useful characterization method for DENs.

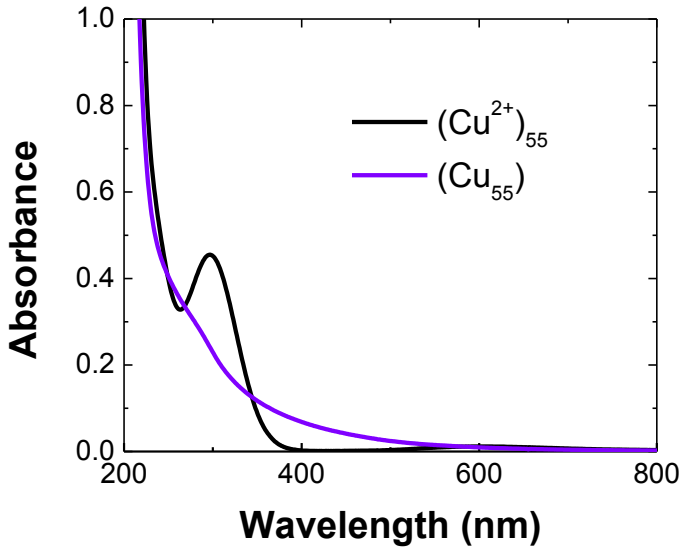

Figure 1.4

UV-vis spectra of $(Cu^{2+})_{55}$ interacting with the dendrimer (G6-OH) and the resulting LMCT (black) and the same sample after reduction with BH_4^- resulting in the formation of a nanoparticle (Cu_{55})(purple). Spectra obtained with a 1.0 cm cuvette and a water blank. The concentration of the G6-OH dendrimer was 2.0 µM.

Electrochemistry also yields information about the identity of metals on the surface of DENs; for example, the presence of hydride waves can be correlated to Pt atoms.[28] More importantly, however, electrochemical measurements make it possible to directly measure electrocatalytic onset potentials and rates for comparison to theory.[29] While these routine techniques contribute to our understanding of DEN structure, an atomic-level understanding is best achieved using extended X-ray absorption fine structure (EXAFS)

spectroscopy, which provides information about the local structure of nanoparticles.[30,31] EXAFS is, however, an averaging technique, so a high degree of monodispersity in size and composition is a prerequisite for deriving meaningful conclusions.[32] DENs meet these criteria, but as with XRD-PDF, synchrotron radiation and data fitting are necessary for obtaining meaningful results.

X-ray Absorbance spectroscopy

In an X-ray absorption spectroscopy (XAS) experiment, the X-ray absorption coefficient, μ(E), is measured as a function of X-ray energy (E) which is scanned through the use of a monochromator. When the energy corresponds to the energy of a core electron being promoted to the continuum, an increase in μ(E) is observed. This is referred to as an adsorption edge. For example, a K edge corresponds to the promotion of a 1s electron. As the binding energies of these core electrons are characteristic to each element, this technique is element specific. We are interested in measuring the changes in μ(E) near the absorption edge, as the surrounding atoms in its coordination sphere interact with the outgoing photoelectron and backscatter, which gives us information about the coordination environment of that atom.[33] EXAFS is an essential analytical technique for evaluating nanoparticles in the 1-2 nm size range. It is an element

specific analysis of atomic ordering. Importantly, EXAFS does not rely on the system having long-range order, as each atom and its corresponding coordination sphere is probed. In this work, two related X-ray absorption spectroscopy techniques are used: EXAFS spectroscopy and X-ray absorption near edge structure (XANES) spectroscopy. The difference in the regions is illustrated in Figure 1.5.

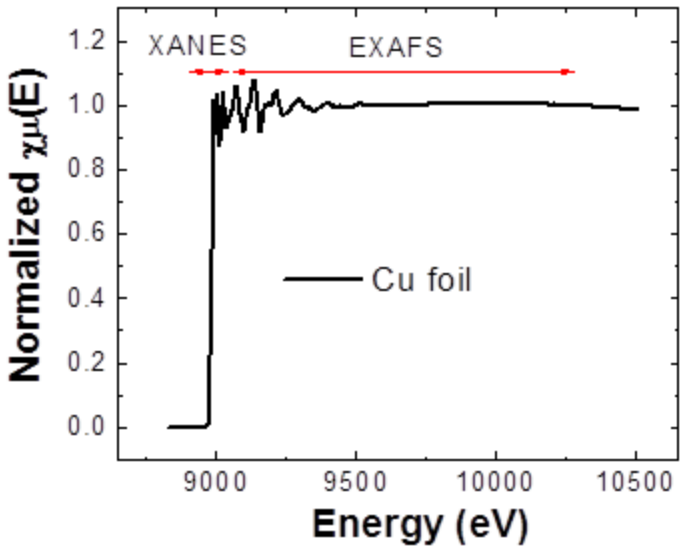

Figure 1.5

X-ray absorption spectrum of a Cu foil. The XANES and EXAFS regions of interests are distinguished.

XANES spectroscopy possesses many of the same attributes as EXAFS, but is also a sensitive probe of oxidation state and can be used as a finger-printing region for comparison to

standards. The height of the white line peak at the absorption edge is dependent on the oxidation state of the material, which makes for good visual identification of changes in oxidation state. This is illustrated in Figure 1.6 where a $CuSO_4$ and a Cu foil are compared. Fitting of XANES data is outside the scope of this dissertation, but linear combination analysis (LCA) is utilized as a means of obtaining quantitative data. As the name suggests, LCA is a linear combination of two or more endmembers (standards) to fit the sample of interest. The percentage of each of these endmembers is then determined. The feasibility of this method relies on the use of appropriate standards. This is difficult when using nanoparticles in the 1-2 nm size range, as there are significant deviations from the bulk materials in the XANES region. In this dissertation, DENs samples are used as the endmembers for LCA fitting to ensure that the samples are well described by the standards, and all other comparisons are only qualitative.

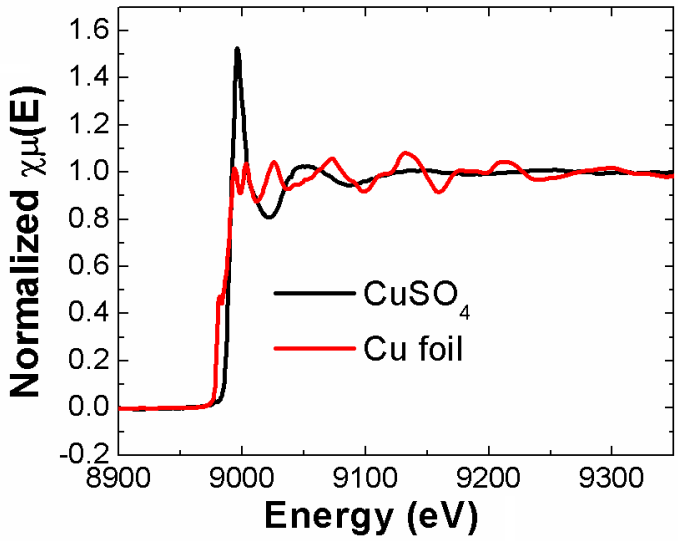

Figure 1.6

XANES spectra of a $CuSO_4$ (black) and a zerovalent Cu foil (red) demonstrating the difference in white line intensity and near-edge features.

Subtractively Normalized Interfacial Fourier Transform Infrared Spectroscopy

Fourier transform infrared (FTIR) spectroscopy is a useful technique for studying the surface structure of heterogeneous catalysts.[34] Adsorbed CO (CO_{ads}) is often used as a structural probe. It binds strongly to Pt surfaces and the C-O stretching mode is IR active. Its stretching frequency, as measured by IR spectroscopy, can be correlated to the binding energy of CO_{ads}. The stretching frequency is well known

to vary with the surface geometry (i.e. Pt(111) versus Pt(100) single crystals).[35] Subtractively Normalized Interfacial Fourier Transform Infrared Spectroscopy (SNIFTIRS) is a strategy that allows for infrared (IR) measurements to be obtained in electrochemical systems.[36] This is an effective technique for probing an adsorbate, in this case CO. Using electrochemical potential control, the potential can be modulated during IR data collection. Typically this is done with a potential at which CO is adsorbed to the surface, and then a potential sufficiently positive at which CO has been desorbed. To minimize the water layer, the configuration depicted in Illustration 1.3 is used. At the base of the in situ cell is a ZnSe total internal reflection (TIR) crystal. The incoming IR beam undergoes TIR at the interface and the evanescent wave produced samples the thin catalyst layer. The signal that arises from the interfacial region of water between the TIR crystal and the electrode can be subtracted in this way, and the signal due to the adsorbate of interest can be isolated.

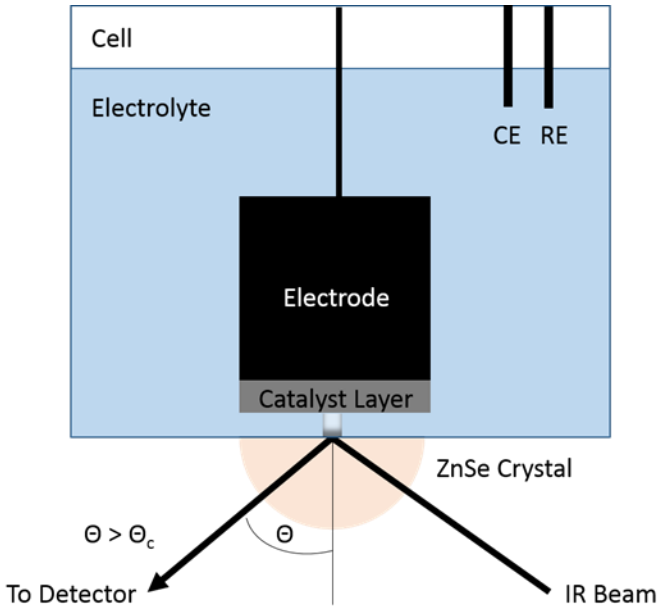

Illustration 1.3

Schematic of the electrochemical cell used for SNIFTIRS measurements, where CE is the counter electrode, RE is the reference electrode. Θ_c is the critical angle for total internal reflection to occur.

Dissertation Overview

In this dissertation the various analytical methods described above will be applied to thoroughly characterize DENs of various structures. This is carried out with the goal of comparison to theory in order to validate the theoretical models, as well as learn more about the structure of these model electrocatalysts. This process begins with the study of the inversion of Pd@Pt core@shell DENs. By EXAFS it was

determined that the Pd@Pt structure is unstable at this size range and that the more noble Pt partitions into the core. This is confirmed by DFT studies of this system. Next, an improved synthesis strategy for Pt DENs is outlined making use of galvanic exchange to achieve complete reduction of the Pt catalyst. These fully reduced Pt DENs are then studied by FTIR to probe the binding of CO to the surface to gain insight into the binding configuration and sites available, as CO binding is an important descriptor for activity predictions. These studies help to join theory and experiment, with the overarching goal of improving catalyst development strategies.

Chapter 2: An Experimental and Theoretical Investigation of the Inversion of Pd@Pt Core@Shell Dendrimer-Encapsulated Nanoparticles[†]

Introduction

Here we report the homogeneous synthesis of core@shell $Pd_{147}@Pt_{162}$ dendrimer-encapsulated nanoparticles (DENs) and the subsequent spontaneous reconfiguration of these structures to yield an inverted $Pt_{147}@Pd_{147}Pt_{15}$ form (the subscripts represent nominal numbers of atoms in the core and shell, Illustration 2.1). Because these DENs undergo structural rearrangements, we will use the notation "PdPt", which does not imply a particular structure, for the as-synthesized DENs, and reserve the more specific core@shell notation "Pd@Pt" for cases where this structure has been confirmed.

[†] Anderson, R. M.; Zhang, L.; Loussaert, J. A.; Frenkel, A. I.; Henkelman, G.; Crooks, R. M. *ACS Nano* 2013, *7*, 9345-9353.
L. Zhang performed the simulations under the supervision of G. Henkelman. J. A. Loussaert helped with data collection. A. I. Frenkel helped with data interpretation. R. M. Crooks was the project supervisor.

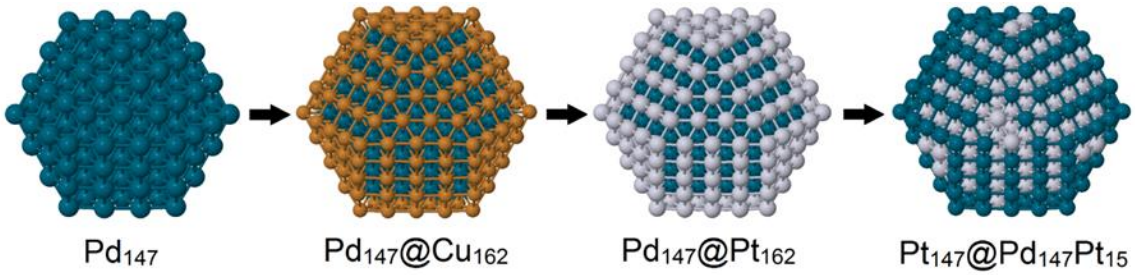

Illustration 2.1

Synthetic scheme showing the synthesis of $Pd_{147}@Pt_{162}$ and the subsequent inversion to form $Pt_{147}@Pd_{147}Pt_{15}$.

We have recently discovered that atomic remodeling of the sort reported here may be relatively commonplace in 1-2 nm nanoparticles,[37,38] whereas structurally similar larger nanoparticles retain stable configurations.[39-41] In addition to the inversion process, which is confirmed experimentally by in situ extended X-ray absorption fine structure (EXAFS) spectroscopy, there are two additional key findings arising from this study. First, the inversion process is also predicted to occur by density functional theory (DFT) calculations. Second, the synthetic approach for preparing these PdPt DENs in homogenous solution has not previously been reported, and it opens the door to preparation of significant quantities of 1-2 nm bimetallic DENs having well-defined structures.

It has been reported that Pd@Pt nanoparticles exhibit enhanced electrocatalytic activity for the oxygen reduction reaction (ORR) compared to monometallic Pt catalysts.[40,42,43] Techniques such as high-resolution scanning transmission electron microscopy (HR-STEM),[41] Fourier-transform infrared spectroscopy (FT-IR),[44,45] and EXAFS[39,46] have been used to investigate the structure and structural stability of Pd@Pt nanoparticles within the size range of 2.0 to 5.0 nm. For example, Chen and coworkers prepared 4.5 nm Pd@Pt nanoparticles using a surface-limited-growth procedure. This is a three-step synthesis in which: (1) Pd nanoparticles are exposed to hydrogen, thereby forming a PdH shell, (2) Cu^{2+} is reduced onto the Pd surface via cross reaction with the hydride, and (3) the $Pd_{147}@Cu_{162}$ nanoparticles are exposed to Pt^{2+}, which leads to galvanic exchange and formation of the final ~4.5 nm product having a Pd core and an ultrathin Pt shell.[39] We used a synthetic strategy similar to this in the present study to prepare ~2 nm $Pd_{147}Pt_{162}$ DENs.

In a study closely related to ours, Russell and coworkers reported the synthesis and structural properties of PdPt nanoparticles.[47] In this case, they started with a commercial carbon-supported Pd catalyst and used a controlled surface reaction (CSR) route to add a Pt shell. Depending on the Pt:Pd ratio, the size of the particles ranged from 2.0 to 3.4 nm.

On the basis of EXAFS and electrochemical analyses, these materials were reported to have a mixed (Pd and Pt) surface composition with Pt preferentially located sub-surface. This rearrangement was explained in terms of previously calculated segregation energies.[48] Other calculations on bimetallic PdPt clusters in this size range also indicate that the most stable configurations have a Pt-rich core.[49-52]

Monometallic DENs are generally prepared by a two-step process.[21,22] First, a solution containing a particular metal-ion:dendrimer ratio is prepared. This results in the metal ions partitioning into the dendrimer interior. Second, a chemical reducing agent, such as BH_4^-, is added to this solution. This leads to formation of a zerovalent metal nanoparticle sterically trapped within the dendrimer. The size of the DEN is strongly correlated to the original metal-ion:dendrimer ratio in the solution prepared in the first step.[53] Importantly, the host dendrimer does not interact strongly with the surface of the encapsulated nanoparticle,[25] which means DENs are catalytically active.

Our present interest is focused on synthesizing bimetallic alloy[54,55] and core@shell[28,56] DENs, and then comparing their catalytic properties to DFT calculations.[38,57,58] There are two critical conditions for such comparisons to be viable. First, the particles must be small

enough to enable direct correlation to computations. Second, the structure of the particles must be very well defined. Both of these conditions are frequently achieved with DENs. However, we have observed some unusual cases that give rise to atypical structures. A case in point is the PdAu DEN system.[37] When a Pd^{2+}/Au^{3+} DEN precursor is co-reduced, stable bimetallic alloy DENs form. If Au^{3+} is loaded into the dendrimer and reduced, and then Pd^{2+} is subsequently added and reduced, stable Au@Pd DENs result. However, if the order of reduction is reversed, a Pd@Au DEN structure is anticipated, but the experimental finding is that the inverted Au@Pd structure results.

These prior observations for PdAu DENs are consistent with the results reported here for the PdPt system. Specifically, nominal $Pd_{147}Pt_{162}$ DENs (2.0 ± 0.2 nm) prepared by the previously discussed synthesis procedure (PdH formation, followed by galvanic exchange first for Cu and then for Pt) were examined by electron microscopy, UV-vis spectroscopy, X-ray photoelectron spectroscopy (XPS), in situ EXAFS, and X-ray absorption near edge structure (XANES) spectroscopy, and the results of all these analytical methods are consistent with structural inversion in which the more noble Pt partitions to the core and the shell becomes enriched in Pd. Moreover, we are now able to rationalize the structural

inversion using first-principles calculations. Specifically, we present comparative thermodynamic stability calculations of different structures and segregation energies derived from swapping core and shell atoms. These calculations make it possible to propose a mechanistic route for the inversion process involving the high-energy corner and edge sites that are numerous only on very small nanoparticles. As noted earlier, larger Pd@Pt nanoparticles have stable structures, presumable due to their much small relative number of corner and edge atoms.

Experimental Section

Chemicals

Sixth-generation, hydroxyl-terminated poly(amidoamine) (PAMAM) dendrimers (G6-OH) in methanol were purchased from Dendritech, Inc. (Midland, MI). The methanol was removed under vacuum and the dendrimers reconstituted in water at a concentration of 250.0 μM. The following chemicals were used as received: K_2PtCl_4 and K_2PdCl_4 were purchased from Acros Organics; $CuSO_4$ and NaOH from Fisher Scientific; and $NaBH_4$ from Sigma-Aldrich. For electrochemical experiments, high-purity $HClO_4$ was purchased from J.T. Baker and high-purity (99.999%) O_2 and Ar gases were purchased from Praxair. All solutions

were made using deionized water having a resistivity of 18.2 MΩ•cm (Milli-Q gradient system, Millipore).

DEN Synthesis

Pd DENs were synthesized as previously reported.[59] Briefly, a 2.0 μM solution of G6-OH PAMAM dendrimer was prepared from a 250.0 μM stock solution. To this, 147 equivalents of K_2PdCl_4 were added from a freshly prepared 0.010 M stock solution, and this solution was stirred for 30 min. Next, a 10-fold excess of $NaBH_4$ was added from a 1.0 M stock solution, and the resulting solution was allowed to stir for 15 min. We refer to these materials as Pd_{147} DENs, where 147 is the metal-ion:dendrimer ratio and also reflects the approximate number of Pd atoms in each DEN. The Pd_{147} solution was then purged with H_2 for 30 min, and while still purging excess unreacted $NaBH_4$ was removed by adding aliquots of a 10% $HClO_4$ solution until the pH of the solution reached ~3.0. Next, aliquots of 0.30 M NaOH were added to raise the pH to ~7.5, and then 162 equivalents of $CuSO_4$ were added with continuous purging of the solution with H_2. After 15 min, the purge gas was changed to N_2 and the solution was purged for an additional 30 min. Finally, 162 equivalents of K_2PtCl_4 were added from a freshly prepared 0.10 M stock solution. The

resulting DENs were kept under N_2 until analysis to ensure their stability.

Characterization

UV-vis spectra were acquired using a Hewlett-Packard HP8453 spectrometer. Transmission electron microscopy (TEM) images were obtained using a JEOL-2010F TEM operating at 200 kV. Samples for TEM analysis were prepared by drying 3 µL of a $Pd_{147}Pt_{162}$ catalyst ink (a mixture of DENs and Vulcan carbon, described later) on a lacey carbon grid. TEM samples of DENs obtained after electrochemical analysis were prepared by wiping the electrode surface with the TEM grid so that a portion of the dried ink was transferred to the grid. The particles were sized using Gatan Digital Micrograph software. XPS analysis was carried out using a Kratos Axis Ultra spectrometer equipped with a monochromatic Al Kα radiation source. The XPS samples were dried on a glassy carbon (GC) chip, and peak positions were normalized to the C1s peak position at a binding energy of 284.5 eV. STEM images and energy-dispersive X-ray spectroscopy (EDS) spectra were acquired on a JEOL JEM-ARM200F aberration-corrected microscope operated at 200 kV.

Electrochemistry

Cyclic voltammograms (CVs) were obtained in a 0.10 M $HClO_4$ electrolyte solution using a Au counter electrode and a Hg/Hg_2SO_4 reference electrode (CH Instruments, Austin, Texas), which was calibrated daily against an eDAQ Hydroflex hydrogen reference electrode. All potentials were converted to, and reported relative to, the reversible hydrogen electrode (RHE) scale. For electrochemical measurements, a CHI 1202B potentiostat (CH Instruments) was used. Rotating disk voltammetry (RDV) employed a Pine Instruments AFASR rotator and E7R9 series GC disk working electrode having a geometric area of 0.248 cm^2.

For electrocatalytic measurements, the electrode surface was modified with a DEN-containing ink prepared by mixing 1.0 mg Vulcan carbon EC-72R per 1.0 mL of a solution containing 80% 2.0 μM DENs, 20% isopropyl alcohol, and 0.05% Nafion. After sonicating this mixture for several minutes, 10 μL of the ink was allowed to dry on the GC disk electrode. For CVs the electrolyte solution was purged with high-purity Ar, and for RDV experiments the solution was purged with high-purity O_2.

X-ray absorption spectroscopy (XAS)

XAS data were collected at beamline X18B at the National Synchrotron Light Source (NSLS) at Brookhaven National Laboratory. Reference foils were collected in transmission mode and the data fit to yield the amplitude factors (S_0^2) that contribute to theoretical EXAFS signals for each absorber (Pt or Pd). An S_0^2 value of 0.89 for the Pd K edge and 0.87 for the Pt L_3 edge were used for analysis. Pd_{147} DENs were prepared at a concentration of 50.0 µM and purged with 5% H_2 in He. After the analysis of the $Pd_{147}@Cu_{162}$ intermediate, the purging gas was changed to pure He to ensure stability of the DENs. For in situ experiments the data were collected in fluorescence mode using a passivated implanted planar silicon (PIPS) detector. The data were analyzed using the IFFEFIT and Horae software packages.[60-62] For analysis of monometallic Pd_{147} DENs and the $Pd_{147}@Cu_{162}$ intermediates under H_2, the Pd K edge was fit with FEFF6 theory[63] in R-space using a k-weight of 2 for the Fourier transforms. For the final structure, simultaneous first-shell fitting of both Pd and Pt edges was done using a k-weight of 2 and by constraining the bond lengths (r) and Debye-Waller factors (σ^2) for the Pd-Pt and Pt-Pd scattering paths to be equivalent as measured from either edge.[64]

Density Functional Theory

DFT was used to calculate segregation energies of $Pd_{147}@Cu_{162}$ and $Pd_{147}@Pt_{162}$. All calculations were performed using the VASP code,[65,66] where electron correlation was evaluated within the generalized gradient approximation using the Perdew-Wang91 functional.[67] Core electrons were described with the projector augmented-wave method.[68,69] Kohn–Sham wave functions for the valence electrons were expanded in a plane wave basis set with an energy cutoff of 280 eV. The energy cutoff was increased to 400 eV, and the segregation energy of $Pd_{147}@Pt_{162}$ was found to vary by less than 0.01 eV. Spin polarization was tested and used as required.

The $Pd_{147}@Pt_{162}$ nanoparticles were modeled as 309 atom face-centered cubic (FCC) crystallites in the shape of a cuboctahedron with 147 core atoms and 162 shell atoms, which is consistent with the size of the synthesized DENs. A cubic box of side length 28 Å was used to contain the particle with a vacuum gap of at least 11 Å in all directions to avoid interactions between periodic images. A Γ-point sampling of the Brillouin zone was used for the isolated particles. All atoms in the nanoparticle were allowed to relax; geometries were considered optimized when the force on each atom was <0.01 eV/Å.

Results and Discussion

Particle synthesis and UV-vis analysis

As described in the Methods Section, G6-OH(Pd_{147}) DENs were prepared by first complexing 147 equivalents of $PdCl_4^{2-}$ to the interior of the dendrimer. The UV-vis spectrum of this precursor (Figure 2.1, black line) displays the expected ligand-to-metal charge transfer (LMCT) band at ~230 nm. After reduction with $NaBH_4$ the LMCT band disappears and the broad-band absorption associated with nanoparticles is observed (red line). Importantly, after the addition of Cu^{2+} in the presence of H_2 gas (blue line), no dendrimer/Cu^{2+} LMCT band is present at λ_{max} = 300 nm,[70] indicating that Cu^{2+} is not complexed to the dendrimer but rather is in its reduced form. The observed increase in the broad absorbance after adding Cu^{2+} is associated with the presence of larger DENs, suggesting that Cu is present as a thin shell on the Pd DENs. After addition of Pt^{2+}, and the corresponding galvanic exchange of Cu for Pt, the absorbance increases again (green line). Again, no dendrimer/Cu^{2+} LMCT is observed, but in this case its absence is due to the low pH (~3) of the solution and the resulting protonation of the interior tertiary amines of the dendrimer.[70] Taken together, the UV-vis results are fully consistent with the proposed synthetic pathway illustrated in

Illustration 2.1, though they do not provide sufficient information to provide structural details about the product.

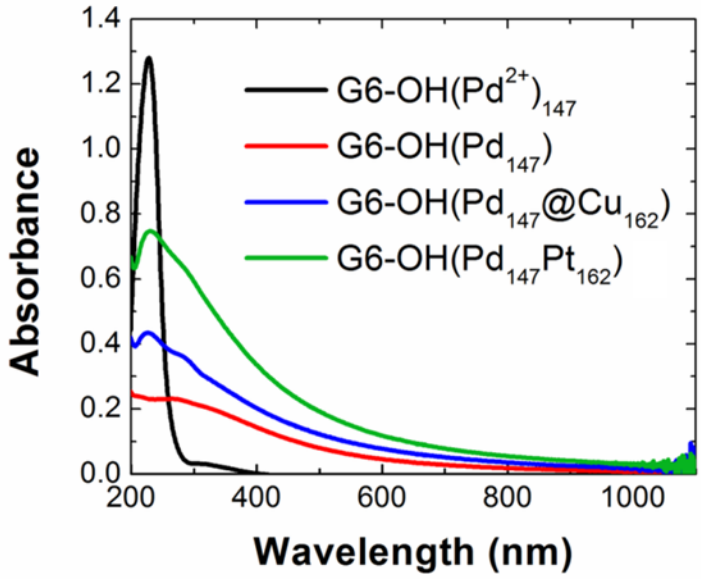

Figure 2.1

UV-vis spectra of each step of the homogeneous synthesis of $Pd_{147}Pt_{162}$ DENs at a concentration of 2.0 μM in a 2.00 mm quartz cuvette, blanked with 2.0 μM G6-OH.

The open circuit potential (OCP) of the synthetic process is also monitored in Figure 2.2. Beginning with a N_2 purged solution, H_2 is introduced and the OCP drops to ~-0.96 V. After the addition of sufficient $CuSO_4$ to yield a 1.0 mM solution, the potential rises to ~0.4 V which is consistent with the nernstian potential of the deposition of Cu. There is only a slight change in potential upon switching back to

N_2 purging. After the addition of sufficient K_2PtCl_4 to yield a 1.0 mM solution, the potential again rises, indicating the deposition of Pt through galvanic exchange. The OCP trace provides support for the hypothesis that a hydride is formed at the Pd DEN. It also demonstrates that the Cu monolayer is stable after switching the purge gas from H_2 to N_2. It also provides insights into the rate of the galvanic exchange process.

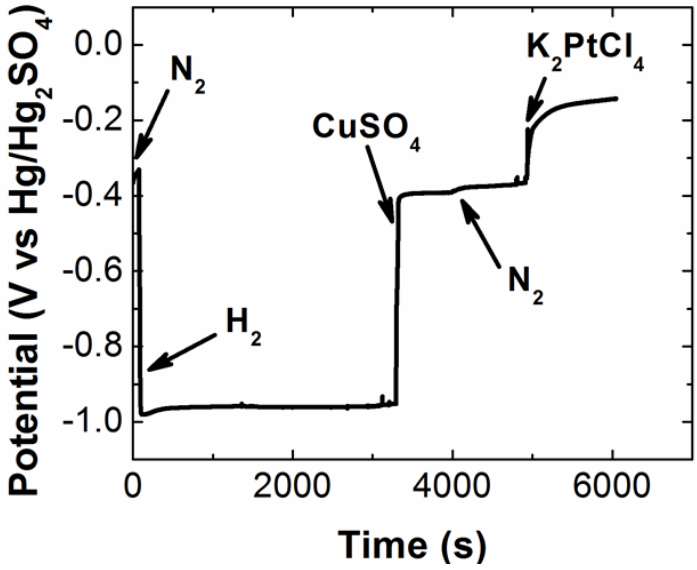

Figure 2.2

Plot of the open circuit potential (OCP) versus time of a GC disk working electrode modified with G6-OH(Pd_{147}) DENs supported on Vulcan carbon in 0.10 M $LiClO_4$ solution.

TEM and XPS analysis of $Pd_{147}Pt_{162}$ DENs

TEM data indicate that the initial Pd_{147} DEN core has a diameter of 1.6 ± 0.2 nm (Figure 2.3), which is consistent with previous reports and the calculated diameter of a 147-atom, closed-shell Pd cuboctahedron.[53]

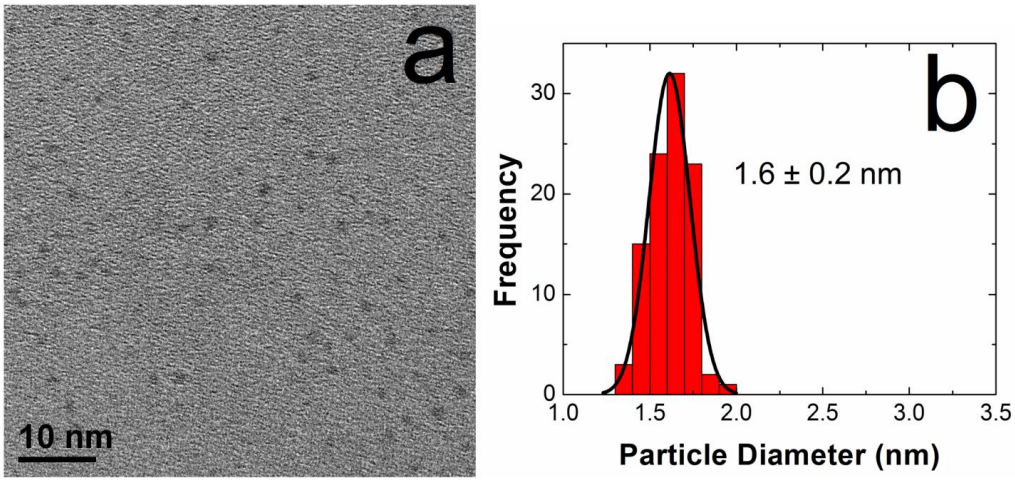

Figure 2.3

(a) TEM image and (b) corresponding size-distribution histogram of monometallic Pd_{147} DENs.

After addition of Pt, however, TEM analysis (Figure 2.4) indicates an average increase in size of 0.4 nm to 2.0 ± 0.2 nm. The expected difference in diameter between Pt particles containing 147 and 309 atoms is 0.45 nm.[71] Note that the micrograph in Figure 2.4a was obtained after immobilizing the

$Pd_{147}Pt_{162}$ DENs onto a Vulcan carbon support (see Experimental Section for details).

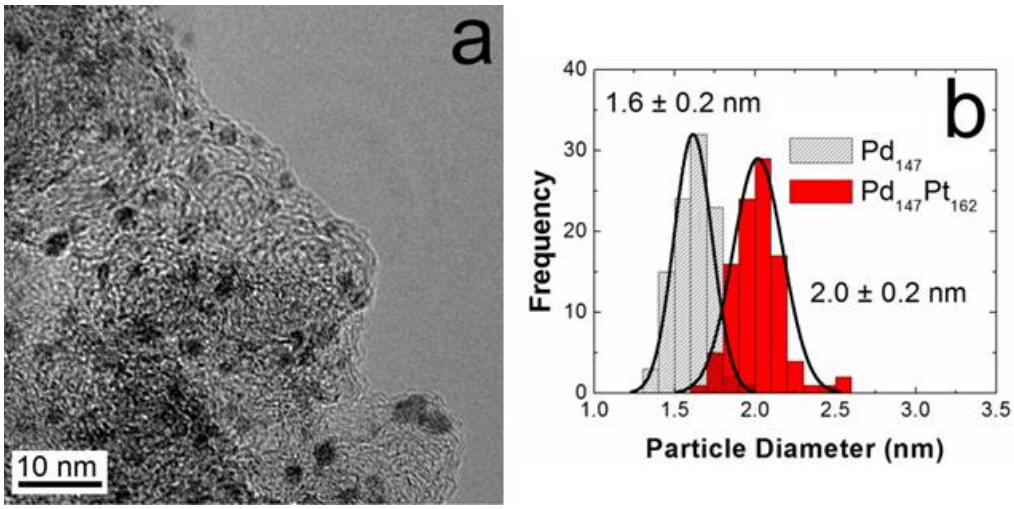

Figure 2.4

(a) TEM image of the $Pd_{147}Pt_{162}$ DENs ink. (b) Size-distribution histogram of the $Pd_{147}Pt_{162}$ DENs and the Pd_{147} DEN precursor showing the 0.4 nm shift in the centroid after addition of Pt.

Figures 3a and 3b show high-resolution STEM images that support the claim of monodispersity in size. Importantly, Figure 3c is an EDS line scan showing that both Pt (red) and Pd (blue) are collocated within the same particle.

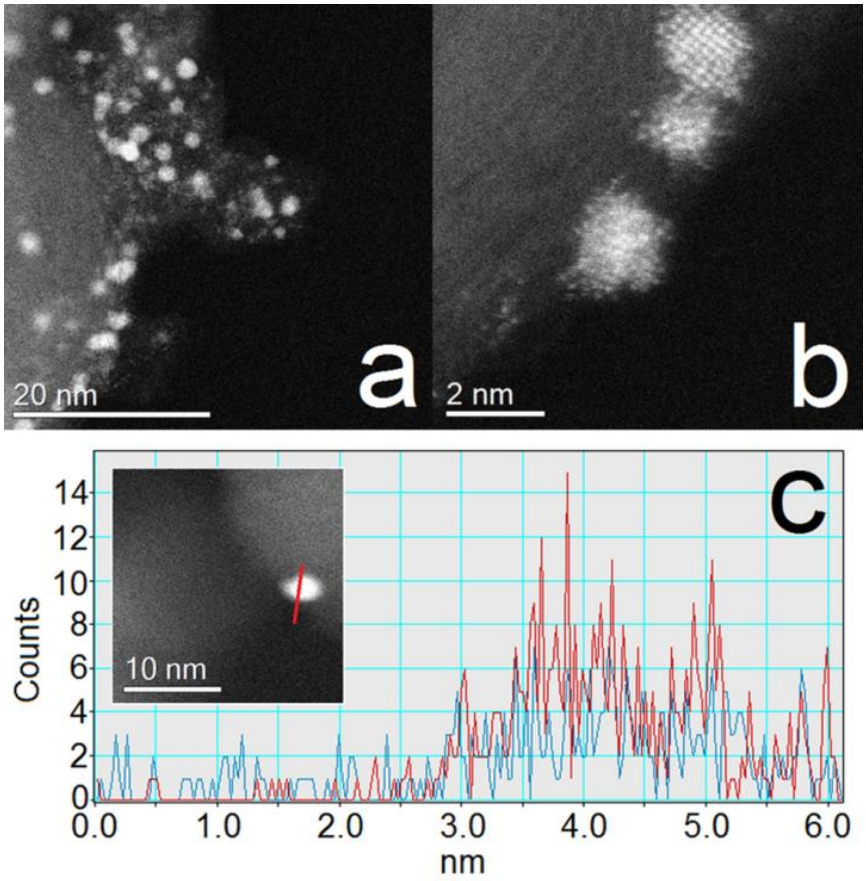

Figure 2.5

a,b) HR-STEM images of $Pd_{147}Pt_{162}$ supported on Vulcan carbon and (c) an EDS line scan of an individual particle indicating collocation of Pt (red) and Pd (blue). The inset shows the particle used for the EDS analysis

Figure 2.6 presents high-resolution XPS scans of the Pd and Pt binding energy region for the $Pd_{147}Pt_{162}$ DENs. For Pd, two peaks are present at 335.6 eV ($3d_{5/2}$) and 341.0 eV ($3d_{3/2}$), which correspond well with those expected for fully reduced Pd DENs: 335.7 eV and 341.0 eV,[59] respectively. This indicates

that Pd is present in its zerovalent form and does not oxidize during synthesis. For comparison, an XPS spectrum of $Pd_{147}Pt_{162}$ DENs that have been intentionally partially oxidized is provided in Figure 2.7. In the partially oxidized DENs, two pairs of peaks are present. One pair corresponds to zerovalent Pd and the other pair, which appear at 338.2 eV and 343.5 eV,[72] correspond to Pd^{2+}. Note that the latter pair of peaks is absent in Figure 2.6a.

Two XPS peaks are also present in the Pt 4f region for the $Pd_{147}Pt_{162}$ DENs (Figure 2.6b). These appear at 71.6 eV ($4f_{7/2}$) and 74.8 eV ($4f_{5/2}$), which is comparable to values previously reported for G6-OH(Pt_{55}) DENs: 71.3 eV and 74.5 eV,[27] respectively. The absence of peaks corresponding to higher oxidation states of Pt indicates that complete galvanic exchange has occurred and that all of the added Pt salt has been reduced. The conclusion that both elements are located within the same nanoparticle and that they are both in their reduced form is necessary to validate the fitting model used for the EXAFS analysis presented later.

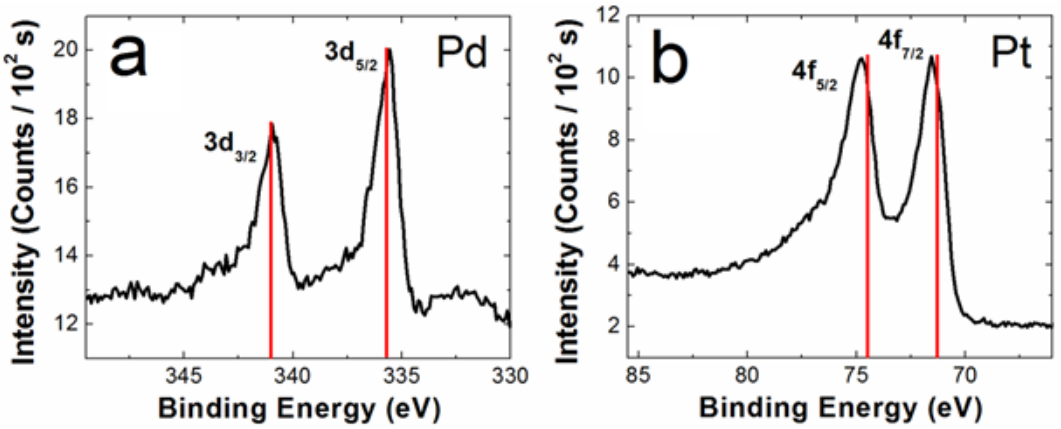

Figure 2.6

High-resolution XPS spectra of $Pd_{147}Pt_{162}$ DENs in the (a) Pd and (b) Pt regions. The solid red lines correspond to the location of the binding energies for the zerovalent metals.

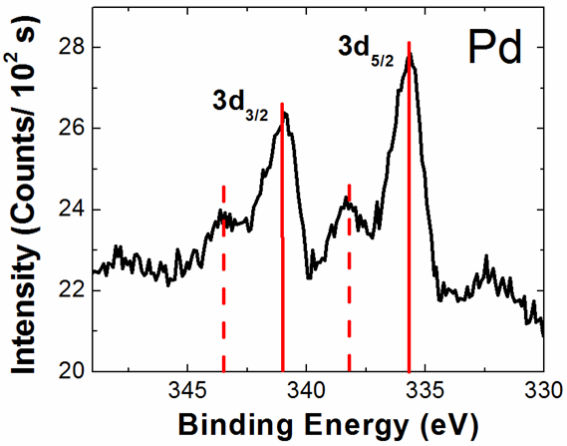

Figure 2.7

High-resolution XPS spectrum of the Pd region for partially oxidized $Pd_{147}Pt_{162}$ DENs. The $Pd_{147}Pt_{162}$ DENs supported on Vulcan carbon were exposed to air for 1 week prior to the measurement. The solid red lines correspond to zerovalent Pd, and the dashed red lines correspond to oxidized Pd (in the form of $PdCl_4^{2-}$).

Electrochemistry

In Figure 2.8, CVs of the $Pd_{147}Pt_{162}$ DENs are compared with those obtained using monometallic Pt_{240} DENs. In each case, the electrode was modified with a DEN-containing ink (see Experimental Section). A CV of the $Pd_{147}Pt_{162}$ DENs (Figure 2.8a) reveals H-atom adsorption and desorption at potentials between 0.3 V and the negative scan limit of 0.05 V. Upon scan reversal, the surface of the DENs is oxidized starting

at ~0.8 V, and then, when the scan is reversed again, the oxide is reduced between 0.8 and 0.5 V. These types of features are characteristic of both monometallic Pd and Pt materials.[40,55,56]

The CV for $Pd_{147}Pt_{162}$ DENs can be compared to that of monometallic Pt DENs. For example, the CV obtained using monometallic Pt_{240} DENs (Figure 2.8b) exhibits two distinct hydride peaks on both the forward and reverse scans. As we have discussed previously, this is a consequence of faceting on larger DENs.[56] The $Pd_{147}Pt_{162}$ DENs exhibit only one adsorption/desorption feature. This has previously been observed in PdPt alloy DENs. In the latter case, increasing Pd content results in a diminution, and eventual elimination, of the second hydride feature.[55] By analogy to these early results, we conclude that the surface of the $Pd_{147}Pt_{162}$ DENs contains a significant amount of Pd.

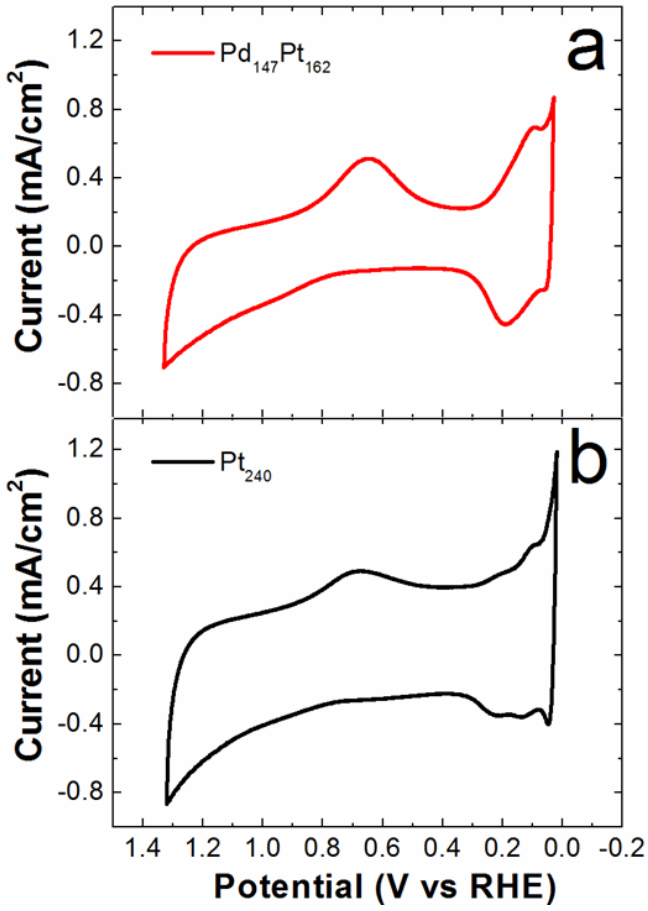

Figure 2.8

CVs of (a) $Pd_{147}Pt_{162}$ and (b) Pt_{240} DENs supported on Vulcan carbon. The scans started at 0.70 V and initially proceeded in the negative direction. The twentieth scans are shown, the scan rate was 100 mV/s, and the electrolyte was Ar-purged.

RDV scans for the ORR at $Pd_{147}Pt_{162}$ and Pt_{240} DENs are compared in Figure 2.9. Here, the onset potential for the ORR at the $Pd_{147}Pt_{162}$ DEN electrocatalysts is shifted slightly negative of the Pt_{240} DENs. In contrast, larger Pd@Pt

core@shell materials exhibit increased activity compared to otherwise equivalent monometallic Pt nanoparticles.[40] Accordingly, the RDV data confirm the CVs and suggest at least some Pd is present on the surface of the $Pd_{147}Pt_{162}$ DENs.

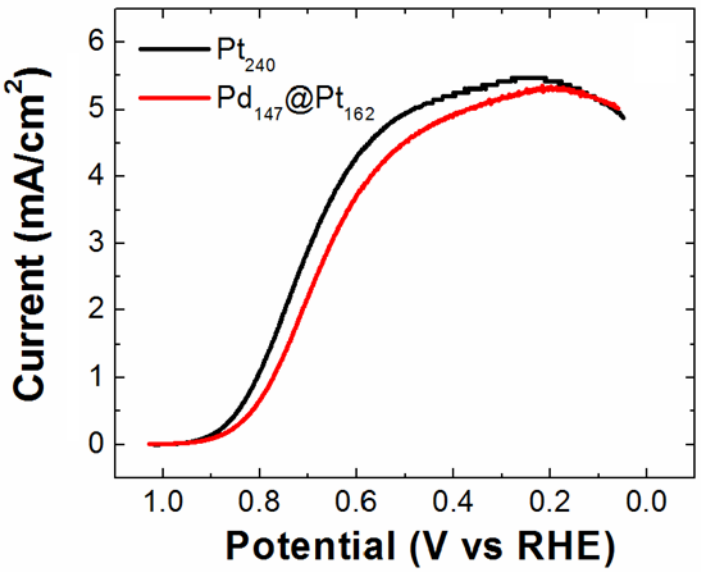

Figure 2.9

RDVs showing reduction of O_2 using the same DEN-modified electrodes that were used for parts a and b. The electrolyte was O_2-saturated 0.10 M $HClO_4$. The scan started at 0.05 V and proceeded at 10 mV/s in the positive direction. The rotation rate was 1600 rpm. All current measurements are normalized to the geometric area of the electrode (0.248 cm^2).

Importantly, the voltammetry of an electrode modified with $Pd_{147}Pt_{162}$ DENs is the same before and after the ORR (Figure 2.10), suggesting that the DEN structure is not altered by the electrocatalytic reduction of O_2. Additional credence for

this claim is provided by TEM images obtained before and after the ORR (Figure 2.11), which show that the average particle size remains unchanged (2.0 ± 0.2 vs. 2.1 ± 0.3, respectively).

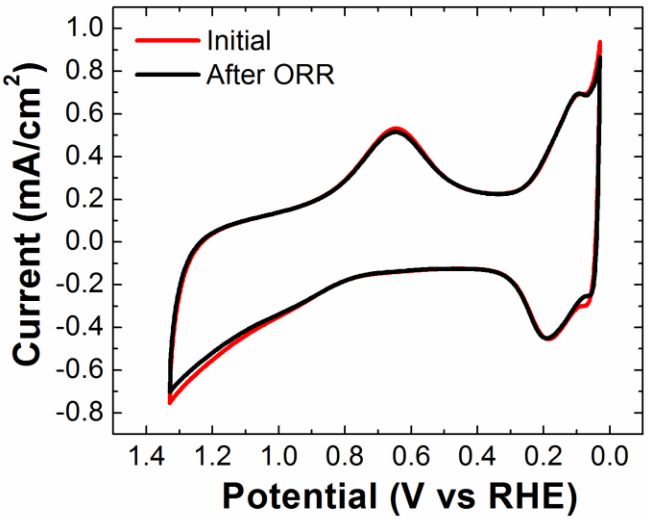

Figure 2.10

Cyclic voltammograms before and after ORR experiments in 0.10 M $HClO_4$. The scan rate was 100 mV/s, the current was normalized to the geometric area of the electrode (0.248 cm^2), and the solution was purged with Ar.

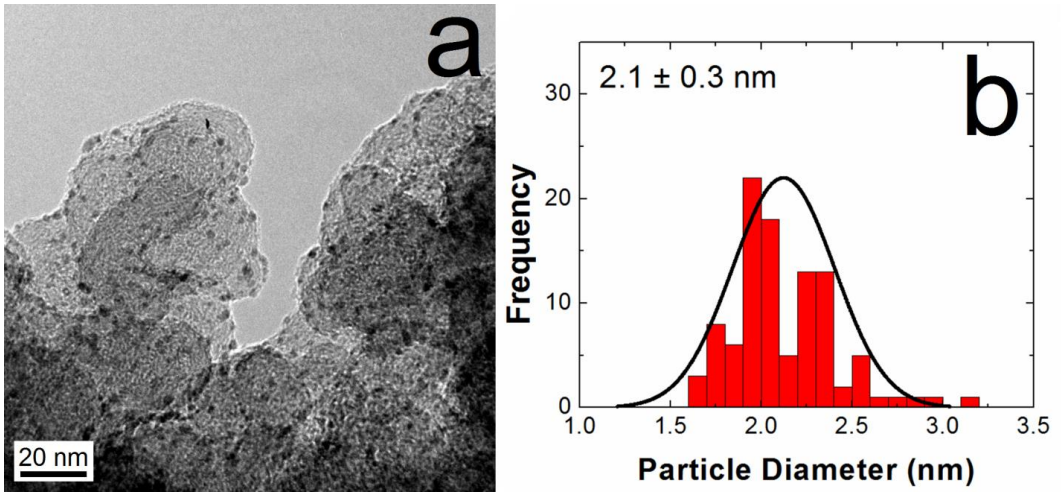

Figure 2.11

(a) TEM image and (b) size-distribution histogram of PdPt DENs after 20 voltammetric scans and ORR RDV testing in 0.10 M $HClO_4$.

In situ XAS structural characterization

Figure 2.12 shows R-space data for the Pd edge of the monometallic precursor Pd_{147} and $Pd_{147}@Cu_{162}$ DENs, as well as the Pd and Pt edges of the $Pd_{147}Pt_{162}$ DENs. Analysis of the Pd EXAFS data for the monometallic Pd_{147} DENs yields a Pd-Pd coordination number (CN_{Pd-Pd}) of 8.4 ± 0.6, which is in good agreement with the calculated value (9.0) for a perfect 147-atom cuboctahedron.

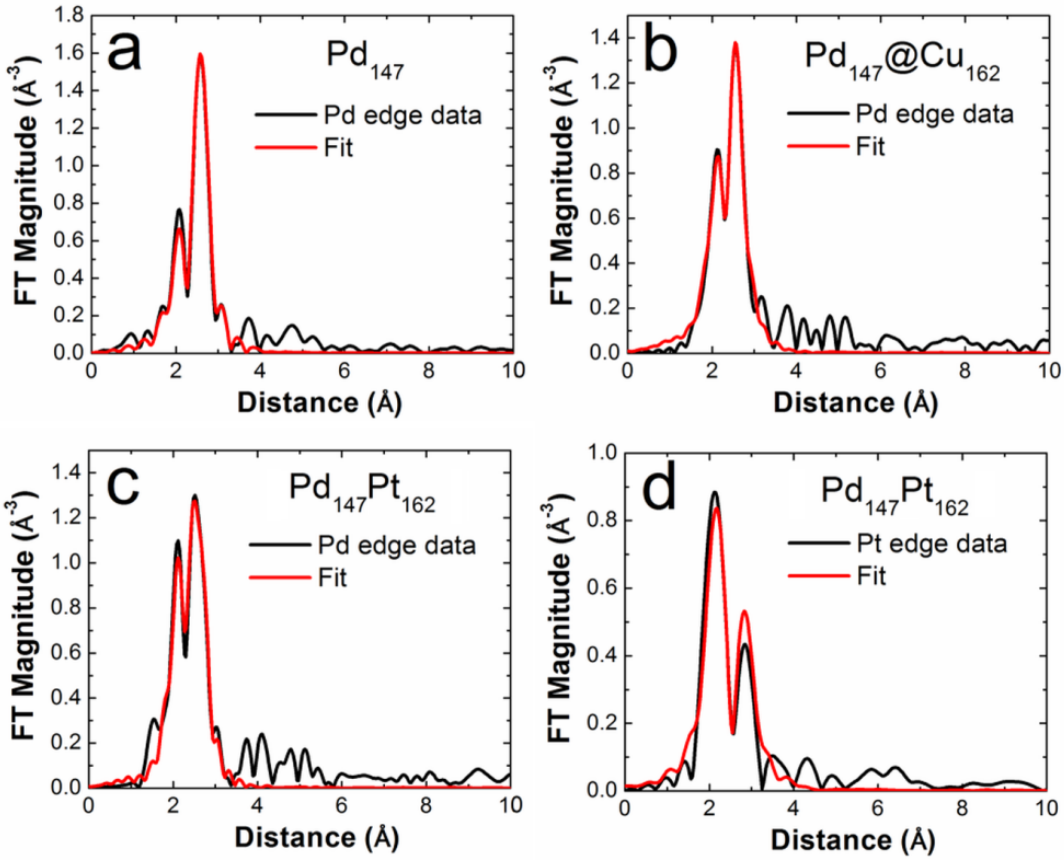

Figure 2.12

EXAFS data and R-space fits (k-weight of 2). (a) Pd edge of monometallic Pd_{147} under H_2; (b) Pd edge of the $Pd_{147}@Cu_{162}$ intermediate under H_2; (c) Pd edge of the final $Pd_{147}Pt_{162}$ DENs under He; and (d) the corresponding Pt edge of the same structure.

Table 2.1 provides Pd-Pd bond length, r_{Pd-Pd}, value of 2.791 ± 0.003 Å, which is larger than for bulk Pd (2.7506 Å). This lattice expansion is probably due to formation of PdH, because the XAS spectrum was obtained in situ during H_2

purging and just prior to addition of Cu^{2+}.[73] After addition of Cu^{2+}, and subsequent reduction, results of the Pd K-edge EXAFS data analysis of the putative $Pd_{147}@Cu_{162}$ intermediate suggest that it maintains a stable core@shell structure. For example, the CN_{Pd-Pd} is, within the uncertainty of the measurement, unchanged in the absence and presence of Cu (8.4 ± 0.6 vs. 7.8 ± 0.7, respectively). If alloying or inversion had occurred, the calculated values from the model structures (Table 2.1) demonstrate that this value would be significantly lower due to reduced Pd-Pd interactions: 4.1 for an inverted particle and 4.6 ± 0.2 for a random alloy. The Pd edge data and fit for the $Pd_{147}@Cu_{162}$ DENs thus confirm the integrity of the Pd core during the Cu deposition step and also indicate some Pd-Cu interactions (CN_{Pd-Cu} = 1.7 ± 0.9).

$Pd_{147}@Cu_{162}$				
	Experimental	Calculated		
CN	$Pd_{147}@Cu_{162}$	$Pd_{147}@Cu_{162}$	$Pd_{147}Cu_{162}$ alloy	$Cu_{147}@Pd_{147}Cu_{15}$
CN_{Pd-Pd}	7.8 ± 0.7	9.0	4.6 ± 0.2	4.1
CN_{Pd-Cu}	1.7 ± 0.9	3.0	5.1 ± 0.2	3.3
$Pd_{147}Pt_{162}$				
	Experimental	Calculated		
CN	$Pd_{147}Pt_{162}$	$Pd_{147}@Pt_{162}$	$Pd_{147}Pt_{162}$ alloy	$Pt_{147}@Pd_{147}Pt_{15}$
CN_{Pd-Pd}	4.8 ± 1.1	9.0	4.6 ± 0.2	4.1
CN_{Pd-Pt}	2.6 ± 1.2	3.0	5.1 ± 0.2	3.3
CN_{Pt-Pt}	10.9 ± 3.7	4.7	5.0 ± 0.2	8.7
CN_{Pt-Pd}	1.3 ± 0.6	2.7	4.6 ± 0.2	3.0

Table 2.1

CNs obtained from the fitting of experimental $Pd_{147}@Cu_{162}$ and $Pd_{147}Pt_{162}$ DENs EXAFS data compared to calculated CNs of model structures. Alloy values are the average of 20 random alloy configurations.

The Cu XANES spectra in Figure 2.13 follow the oxidation state of Cu throughout the in situ synthesis of $Pd_{147}Pt_{162}$ DENs. The first step in this process is reduction of the $CuSO_4$ salt by the hydrided Pd DENs. The most notable observation is that the spectrum for Cu present in the $Pd_{147}@Cu_{162}$ structure (Figure

2.13a, red) lacks the large white line component (compare to Figure 2.13b, black line), indicating that the Cu has been reduced. The XANES spectrum of Cu in the $Pd_{147}@Cu_{162}$ DENs is overlaid with that of a Cu reference foil in Figure 2.13a. For the $Pd_{147}@Cu_{162}$ DENs there are oscillations in the EXAFS region indicative of nearest neighbor scattering. However, the oscillations are not as pronounced as in the case of bulk Cu which has extended order not present in nanoparticles of this size. The final step of the synthesis of the $Pd_{147}Pt_{162}$ DENs is galvanic exchange Cu for Pt. This involves oxidation of the Cu shell back to Cu^{2+}. The Cu XANES spectrum obtained after this step (Figure 2.13b, red) overlays with the $CuSO_4$ standard (Figure 2.13b, black), indicating that the galvanic exchange reaction goes to completion.

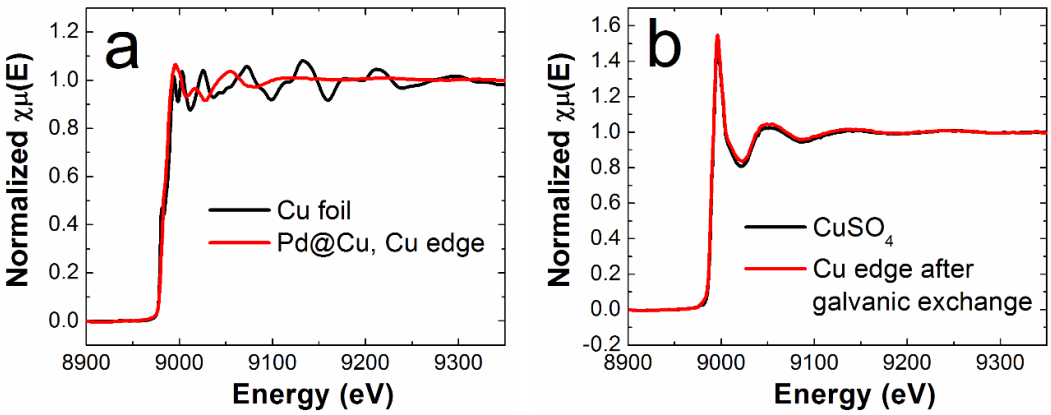

Figure 2.13

Cu XANES of (a) a Cu foil and the reduced Cu shell of the $Pd_{147}@Cu_{162}$ structure; and (b) a $CuSO_4$ solution (no dendrimer present) and the $Pd_{147}Pt_{162}$ DENs solution after the galvanic exchange step. The results indicate that the Cu shell is oxidized in the presence of Pt^{2+}.

The bottom part of Table 2.1 shows CNs extracted from EXAFS data for the $Pd_{147}Pt_{162}$ final product. These data were obtained from the simultaneous first-shell fitting of the Pd and Pt edges. The experimentally determined CN values are compared to three theoretical structures: $Pd_{147}@Pt_{162}$, a $Pd_{147}Pt_{162}$ alloy, and an inverted $Pt_{147}@Pd_{147}Pt_{15}$ structure. The EXAFS data were found to most closely match the inverted $Pt_{147}@Pd_{147}Pt_{15}$ structure. Most strikingly, the CN_{Pt-Pt} (10.9 ± 3.7) is much larger than would be expected for a complete Pt shell (calculated CN_{Pt-Pt} = 4.7) or if the structure was alloyed (calculated CN_{Pt-Pt} = 5.0 ± 0.2). Also, the total Pt-metal CN

(CN_{Pt-M}) of 12.2 (the sum of CN_{Pt-Pt} and CN_{Pt-Pd}) is larger than the total Pd-metal CN (CN_{Pd-M}) of 7.4 (the sum of CN_{Pd-Pd} and CN_{Pd-Pt}). This implies that Pt is more fully coordinated than Pd, which would be expected if Pt is predominantly in the interior of the nanoparticle as surface atoms have fewer nearest neighbors.[64] A full summary of the extracted parameters from the EXAFS fits, including r and σ^2 values, can be found in Table 2.2 for all samples. A TEM micrograph of the $Pd_{147}Pt_{162}$ DENs prepared in situ is presented in Figure 2.14.

Pd_{147}			
	CN_{Pd-Pd}	r_{Pd-Pd} (Å)	σ^2_{Pd-Pd} (Å^2)
Pd	8.4 ± 0.6	2.791 ± 0.003	0.0084 ± 0.0005
$Pd_{147}@Cu_{162}$			
	CN_{Pd-Pd}	r_{Pd-Pd} (Å)	σ^2_{Pd-Pd} (Å^2)
	7.8 ± 0.7	2.752 ± 0.005	0.010 ± 0.002
Pd	CN_{Pd-Cu}	r_{Pd-Cu} (Å)	σ^2_{Pd-Cu} (Å^2)
	1.7 ± 0.9	2.64 ± 0.02	0.006 ± 0.005
$Pd_{147}Pt_{162}$			
	CN_{Pd-Pd}	r_{Pd-Pd} (Å)	σ^2_{Pd-Pd} (Å^2)
Pd	4.8 ± 1.1	2.72 ± 0.01	0.005 ± 0.001
	CN_{Pd-Pt}	r_{Pd-Pt} (Å)	σ^2_{Pd-Pt} (Å^2)
	2.6 ± 1.2	2.72 ± 0.02	0.003 ± 0.002
	CN_{Pt-Pt}	r_{Pt-Pt} (Å)	σ^2_{Pt-Pt} (Å^2)
Pt	10.9 ± 3.7	2.72 ± 0.02	0.011 ± 0.004
	CN_{Pt-Pd}	r_{Pt-Pd} (Å)	σ^2_{Pt-Pd} (Å^2)
	1.3 ± 0.6	2.72 ± 0.02	0.003 ± 0.002

Table 2.2

Table of all extracted EXAFS fit parameters for Pd_{147}, $Pd_{147}@Cu_{162}$, and $Pd_{147}Pt_{162}$ DENs.

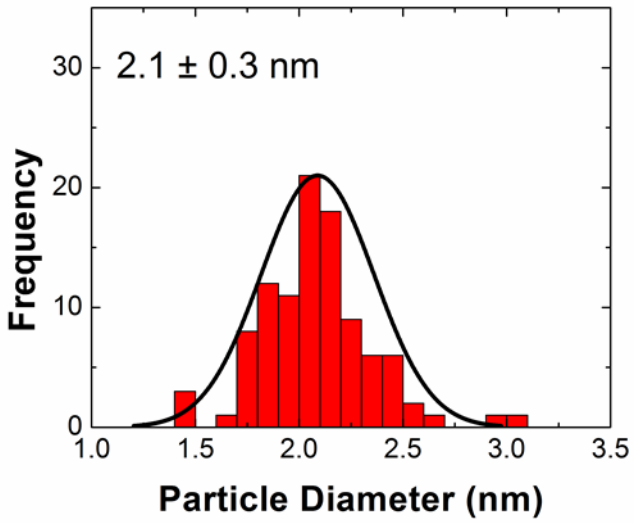

Figure 2.14

TEM size-distribution histogram for $Pd_{147}Pt_{162}$. These data were obtained using DENs synthesized in situ for the EXAFS and XANES experiments, and therefore they correlate exactly to the results shown in Figures 6 and 7 in the main text. TEM samples were prepared by allowing 3.0 µL of the synthesized DENs solution, diluted to 2.0 µM, to dry on a carbon-coated Cu grid (Electron Microscopy Sciences.

DFT calculations

DFT calculations were used to better understand the observed inversion of $Pd_{147}Pt_{162}$ DENs. The thermodynamic stability of $Pd_{147}@Pt_{162}$ nanoparticles was evaluated using the segregation energy (E_{seg}), which is the energy required to swap a shell atom with its neighboring Pd-core atom. Negative values of E_{seg} correspond to favorable exchange of atoms between the shell and core. The effect of an aqueous

environment was taken into consideration by adsorbing a hydroxyl group (OH) to surface sites neighboring the swapped atom. Because Cu binds OH more strongly than Pd, the Cu shell is stabilized and the $Pd_{147}@Cu_{162}$ structure is predicted to be stable. This is the same result found in the aforementioned experiments.

Here we focus on the inversion of $Pd_{147}Pt_{162}$ DENs. The segregation energy for different sites on $Pd_{147}@Pt_{162}$ and Pd/Pt bulk are listed in Table 2.3. For $Pd_{147}@Pt_{162}$ in vacuum, the corner site has the most negative segregation energy (-0.26 eV), indicating that Pt atoms at corner sites are the least stable with respect to migration into the core. The presence of adsorbed OH groups does not significantly change the value of E_{seg} for the (100) facet, or the edge and corner sites. However, E_{seg} of atoms on the (111) facet, which is energetically unfavorable for swapping in the vacuum, drops to -0.27 eV in the presence of OH, becoming another reactive site for core-shell inversion.

	$Pd_{147}Pt_{162}$				Pd/Pt Bulk	
Site	(111)	(100)	Edge	Corner	(111)	(100)
E_{seg} (eV)	0.04	-0.17	-0.06	-0.26	0.03	-0.18
$E_{seg(OH)}$ (eV)	-0.27	-0.11	-0.05	-0.27	-0.28	-0.11

Table 2.3

Summary of segregation energies of $Pd_{147}Pt_{162}$ compared to bulk Pd/Pt, with and without surface hydroxyl present.

Previous studies showed that Pt can form a stable monolayer on a bulk Pd surface and on large (~3.5-9 nm) Pd nanoparticles[39-42,46,74] Accordingly, the same thermodynamic stability calculations used for the DENs, with and without surface OH groups, were performed on 4-layer, 4×4 Pd(111) and Pd(100) slab models supporting a Pt monolayer. The calculated segregation energies of both bulk facets are almost the same (within 0.01 eV, Table 2.3) as for the DEN model. This calculation indicates the inversion we observed on $Pd_{147}Pt_{162}$ is likely due to the unstable corner sites. Within the context of this model, as the size of the nanoparticle increases, the ratio of corner sites to surface sites drops, and the inversion will be less likely to occur. In addition, a Pt monolayer on larger Pd particles is likely kinetically stabilized. The nanoparticles in this study are only 2 nm in diameter, and hence have a relatively flexible structure as

compared to bulk materials, which is expected to lower the barrier for atom swapping especially at low coordinated sites.

$Pd_{55}Pt_{92}$ DENs

To test for generality, we prepared $Pd_{55}Pt_{92}$ DENs using the same approach used for the previously discussed $Pd_{147}Pt_{162}$ DENs. The starting material for this synthesis was G6-OH(Pd_{55}) DENs, a shell of Cu was added, and then the Cu was exchanged for Pt. UV-vis spectra (Figure 2.15) show the same trends as for the $Pd_{147}Pt_{162}$ DENs, and TEM images and sizing histograms indicate an average particle diameter of 1.7 ± 0.2 nm (Figure 2.16) for $Pd_{55}Pt_{92}$.

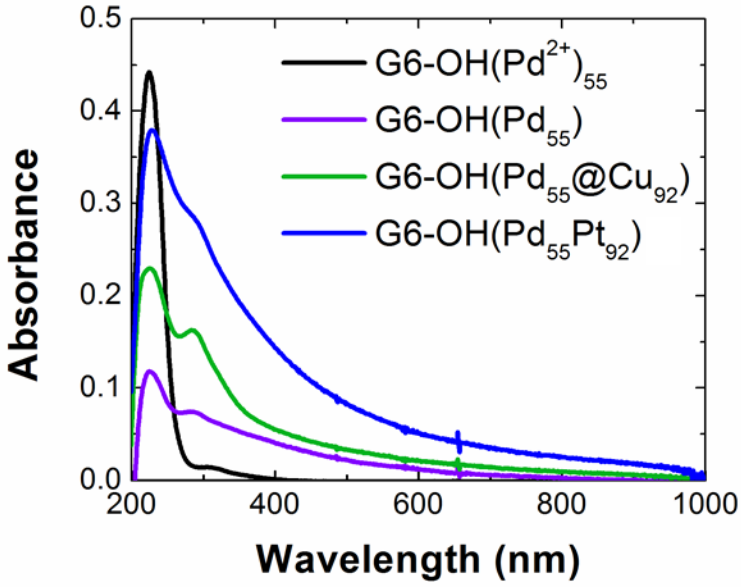

Figure 2.15

UV-vis spectra of each step of the homogeneous synthesis of 2.0 µM $Pd_{55}Pt_{92}$ DENs. The spectra are referenced to a solution containing 2.0 µM G6-OH. The path length of the quartz cuvette was 2.00 mm.

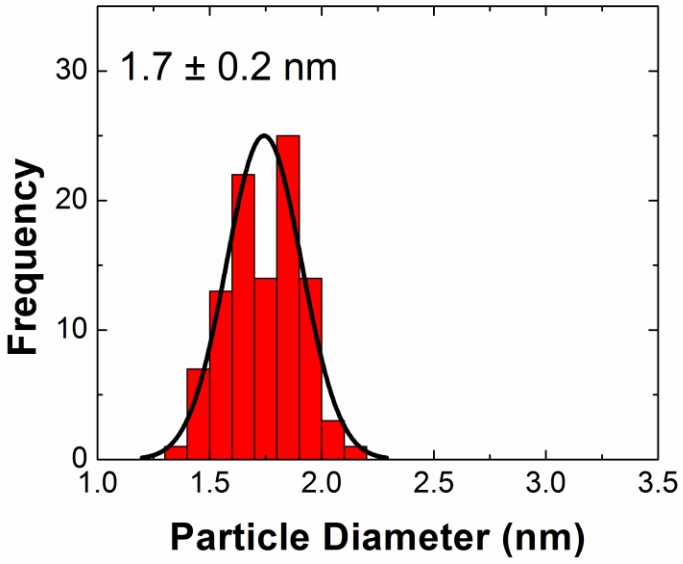

Figure 2.16

TEM size-distribution histogram for 100.0 µM $Pd_{55}Pt_{92}$ DENs synthesized *in situ* for EXAFS experiments. TEM samples were prepared by first diluting the 100.0 µM DENs solution to 2.0 µM, and then pipetting 3.0 µL of the diluted solution onto a carbon-coated Cu grid (Electron Microscopy Sciences).

EXAFS characterization was also performed on the final product of a homogenous solution of $Pd_{55}Pt_{92}$ DENs at a concentration of 100.0 µM. The spectra were obtained under He gas to prevent oxidation, and R-space data and corresponding fits are presented in Figure 2.17. Extracted CNs (Table 2.4) indicate the inversion also occurs with this smaller size of DENs. As for the larger DENs, the most notable EXAFS result is the CN_{Pt-Pt} of 8.1 ± 1.9, which is significantly higher than

anticipated for a $Pd_{55}@Pt_{92}$ core@shell configuration (4.7). Table 2.5 contains a full summary of the extracted parameters from the EXAFS fits of the $Pd_{55}Pt_{92}$ DENs.

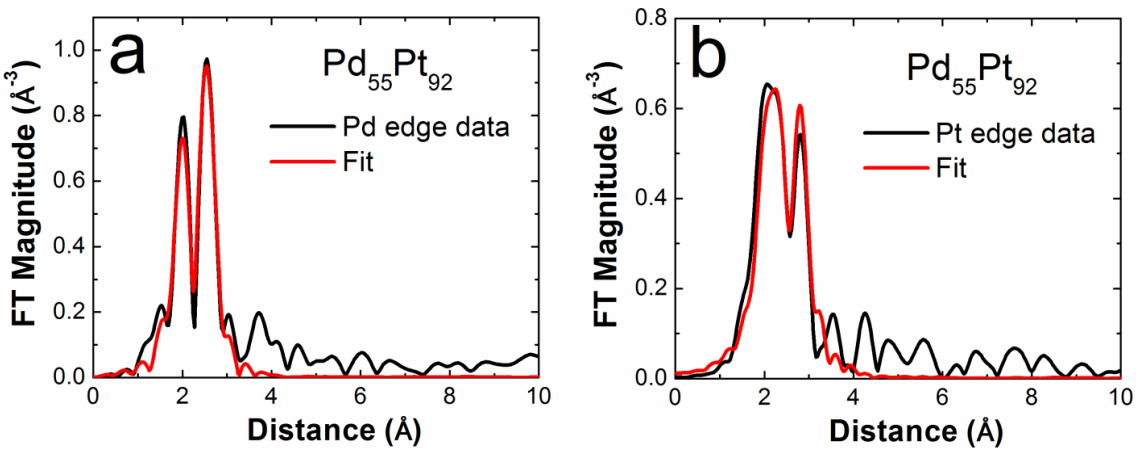

Figure 2.17

EXAFS data and fits in R-space (k-weight of 2). (a) Pd edge of the $Pd_{55}Pt_{92}$ DENs, and (b) the corresponding Pt edge. The data were obtained in a He-purged solution and at a DENs concentration of 100.0 µM.

$Pd_{55}Pt_{92}$				
	Experimental	Calculated		
CN	$Pd_{55}Pt_{92}$	$Pd_{55}@Pt_{92}$	$Pd_{55}Pt_{92}$ alloy	$Pt_{55}@Pd_{55}Pt_{37}$
CN_{Pd-Pd}	3.6 ± 1.5	7.9	3.4 ± 0.3	2.9
CN_{Pd-Pt}	4.0 ± 2.2	4.1	5.6 ± 0.2	3.9
CN_{Pt-Pt}	8.1 ± 1.9	4.7	5.6 ± 0.2	7.9
CN_{Pt-Pd}	1.5 ± 1.0	2.5	3.5 ± 0.1	2.4

Table 2.4

CNs extracted from the EXAFS fits for $Pd_{55}Pt_{92}$ as compared to different model structures. The best agreement is obtained for the inverted $Pt_{55}@Pd_{55}Pt_{37}$ structure.

$Pd_{55}Pt_{92}$			
	CN_{Pd-Pd}	r_{Pd-Pd} (Å)	σ^2_{Pd-Pd} (Å^2)
Pd	3.6 ± 1.5	2.72 ± 0.02	0.005 ± 0.003
	CN_{Pd-Pt}	r_{Pd-Pt}(Å)	σ^2_{Pd-Pt} (Å^2)
	4.0 ± 2.2	2.72 ± 0.03	0.008 ± 0.005
	CN_{Pt-Pt}	r_{Pt-Pt} (Å)	σ^2_{Pt-Pt} (Å^2)
Pt	8.1 ± 1.9	2.71 ± 0.02	0.009 ± 0.001
	CN_{Pt-Pd}	r_{Pt-Pd} (Å)	σ^2_{Pt-Pd} (Å^2)
	1.5 ± 1.0	2.72 ± 0.03	0.008 ± 0.005

Table 2.5

Table of all extracted EXAFS fit parameters for $Pd_{55}Pt_{92}$.

SUMMARY AND CONCLUSIONS

In this paper we have shown that bimetallic DENs can be prepared by a homogeneous route involving sequential

formation of a Pd core, a Cu shell, and then galvanic exchange of the Cu shell for Pt. We anticipated that this approach would yield a Pd@Pt core@shell DEN. However, all of the evidence presented in this paper suggests that the structure inverts into one that is Pt rich in the interior and Pd rich on the exterior. The EXAFS results, in particular, are quite clear on this point.

DFT calculations suggest that the high energy edge and corners sites present in these smaller nanoparticles may help initiate rearrangement to more stable structures. Additionally, the intrinsic disorder present in particles in this size range may contribute to this tendency to reorganize while in bulk systems or in larger nanoparticles the Pt monolayer may be kinetically stabilized. The mechanism of this rearrangement poses an interesting theoretical question and further investigation into this model system is a future direction of this research.

From the results in this study, and our earlier examination of PdAu DENs,[37] we conclude that inversion, and structural instabilities generally, are characteristic of nanoparticles having sizes of <~2-3 nm. These findings are important, because they suggest that in this size range slab models may not be appropriate for nanoparticles. This in turn points to the importance of directly comparing theory with

exact (or nearly exact) experimental models for nanoparticles in this size range.

Chapter 3: Multistep Galvanic Exchange Synthesis Yielding Fully Reduced Pt Dendrimer-Encapsulated Nanoparticles[‡]

Introduction

Dendrimer-encapsulated nanoparticles (DENs) are well-defined nanoparticles having sizes ranging from just a few atoms[23] to perhaps 300 atoms.[21,22] This is the most scientifically interesting range of metal particle sizes because the addition of just a few atoms can drastically change their optical, electrical, mechanical, and catalytic properties.[75-78] For fundamental studies of catalytic properties, DENs are particularly useful for two reasons. First, it is possible to control their size, composition, and structure over a fairly broad parameter space, which is important for comparing theoretical calculations with experimental data.[29,79,80] Second, the presence of the dendrimer protects the particles from agglomeration without poisoning the metal surface. For both of these reasons, DENs are one of the best model materials available for studying the

---

[‡] Anderson, R. M.; Yancey, D. F.; Loussaert, J. A.; Crooks, R. M. *Langmuir* 2014, *30*, 15009-15015.
D. F. Yancey and J. A. Loussaert aided with data collection and interpretation. R. M. Crooks was the project supervisor.

fundamental properties of electrocatalytic reactions on metal particles in the 1-2 nm size range.

Pt is one of the most important catalytic metals, and hence Pt DENs have been studied as catalysts for homogeneous,[81,82] heterogeneous,[83] and electrocatalytic[84-86] reactions. However, we[27] and others[87-90] have previously pointed out that correlations between theory and experiment with DENs are complicated by incomplete reduction of the Pt salt used as the nanoparticle precursor. This situation is unique to Pt DENs and is a consequence of the method used to prepare them. Pt DENs, and DENs in general, are usually synthesized in two steps.[21,22] First the poly(amidoamine) (PAMAM) dendrimer and precursor metal salt are mixed together, and this results in encapsulation of the precursor within the dendrimer interior. Second, a strong reducing agent like BH_4^- is added to the resulting solution. This leads to reduction of the precursor and subsequent intradendrimer agglomeration of the resulting atoms to yield the final nanoparticle.

For most metals, the addition of BH_4^- results in complete reduction of the precursor metal salt. Pt is unusual, however, in that the synthesis leads to a bimodal distribution of fully reduced DENs and fully unreduced, Pt^{2+}-containing dendrimers.[27] This observation is depicted in Illustration 3.1.

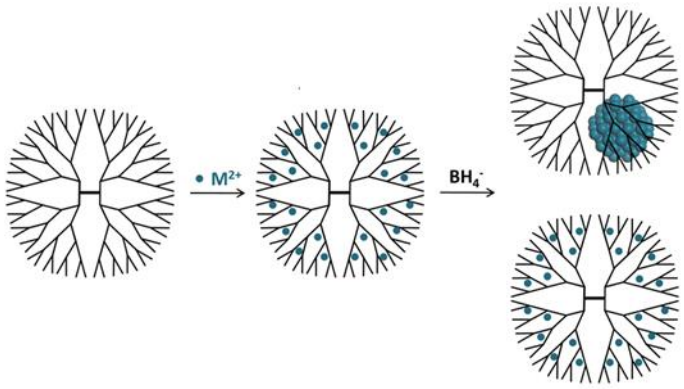

Illustration 3.1

Schematic of the bimodal distribution of fully reduced nanoparticles and fully unreduced complexes that result from reduction with BH_4^-.

We explained this observation by invoking a nucleation and growth mechanism for Pt DENs. Within this framework, zerovalent Pt seeds form in some dendrimers but not in others. In the presence of seeds, additional reduction of Pt^{2+} within that dendrimer is autocatalytic. However, if no seed forms, then the metal salt is kinetically trapped in its oxidized form. At this point we do not know with certainty why seeds form in some dendrimers and not in others, but the problem has been studied by others.[87-89,91] For example, Borodko et al.[88] reported that multidentate binding of Pt^{n+} to amine groups within the dendrimer hinders the reduction of the precursor complex to zerovalent particles, presumably by shifting the redox potential of Pt^{n+} negative. Subsequently, this same

group showed that UV irradiation of the precursor can yield linear Pt chains containing 2-8 atoms, and that these seeds lead to the formation of nanocrystals.[89]

We have shown that small (~1.5 nm), fully reduced Pt DENs can be prepared using the method of galvanic exchange.[92] These materials are prepared by synthesizing Cu DENs using the usual BH_4^- reduction method, and then a Pt salt, such as $PtCl_4^{2-}$, is added to the solution. Because of their relative reduction potentials, the Cu DENs are oxidized to Cu^{2+}, and the Pt salt is reduced to zerovalent Pt.[70] Although this method is highly effective, the largest Pt DENs that can be formed in sixth-generation PAMAM dendrimers by galvanic exchange contain just 64 atoms. This is a consequence of the fact that maximum number of Cu^{2+} ions that can be sequestered within the dendrimer is 64, as shown in Figure 3.1, and that the Cu:Pt galvanic exchange stoichiometry is 1:1.[93] Clearly, it would be advantageous to use this same approach to prepare larger Pt DENs so that a broader size range of materials could be reliably synthesized.

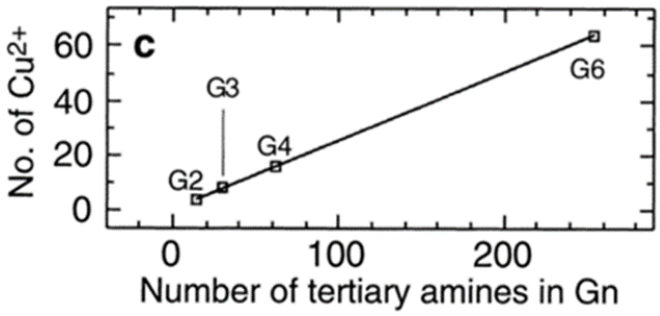

Figure 3.1

The relationship between the number of Cu^{2+} ions complexed to the number of tertiary amine groups within different generations of hydroxyl terminated PAMAM dendrimers. *J. Phys. Chem. B* 2005, *109*, 692-704. Copyright 2005 American Chemical Society.

In the present report, we use more advanced characterization tools, primarily scanning transmission electron microscopy (STEM) and X-ray absorption near edge structure (XANES) spectroscopy, to confirm that the standard BH_4^--reduction method leads to a bimodal distribution of reduced and unreduced Pt-dendrimer composite materials. More importantly, however, we describe a galvanic exchange-based synthetic procedure that leads to larger, fully reduced Pt DENs. The synthetic approach involves two steps. First, Cu DENs containing more than 64 atoms are prepared by carrying out multiple sequential complexation/reduction steps. Second, galvanic exchange of these larger Cu DENs with Pt^{2+} results in Pt DENs containing up to at least 225 atoms. We confirm that full reduction of Pt has occurred using UV-vis

spectroscopy, X-ray photoelectron spectroscopy (XPS), and extended X-ray absorption fine structure (EXAFS) spectroscopy. This advance in the synthesis of model Pt DENs will allow for more accurate comparison of experimental properties to theory, which is the goal of our research in this field.

Experimental Section

Chemicals

Sixth-generation, hydroxyl-terminated (G6-OH) poly(amindoamine) (PAMAM) dendrimers in methanol were purchased from Dendritech (Midland, MI). Before use, the dendrimer solution was dried under vacuum and reconstituted in water at a concentration of 100.0 µM. Isopropyl alcohol and $NaBH_4$ were purchased from Sigma-Aldrich, K_2PtCl_4 was from Acros Organics, $CuSO_4$ and NaOH from Fisher Scientific, high-purity $HClO_4$ from J.T. Baker, and Vulcan carbon was from ElectroChem, Inc. (Woburn, MA). All solutions were made using deionized water having a resistivity of 18.2 MΩ•cm (Milli-Q gradient system, Millipore).

Synthesis of Pt DENs by BH_4^- reduction

The Pt-dendrimer precursor complexes (G6-OH$(Pt^{2+})_n$, *n* = 55, 140, or 225) were prepared by allowing the appropriate amount (55, 140, or 225 equiv., respectively) of K_2PtCl_4 to complex with the interior of G6-OH (2.0 μM) for 72 h. The G6-OH$(Pt^{2+})_n$ precursor was reduced by adding 50 equiv. of $NaBH_4$, and then tightly sealing the container for 24 h. To avoid high H_2 pressures, 15 mL samples of DENs were reduced in 20 mL vials. Note that in the past we have typically used a $NaBH_4$:Pt^{2+} ratio of 10:1, but it was increased here to facilitate maximum Pt^{2+} reduction. UV-vis spectra were acquired using a Hewlett-Packard HP8453 spectrometer. A 2.0 mm quartz cuvette was used and blanked with 2.0 μM G6-OH.

Synthesis of Pt DENs by galvanic exchange

The first step of the Pt DEN galvanic exchange synthesis is preparation of 55-atom Cu DENs using a previously reported procedure.[70,92,93] Briefly, a 2.0 μM solution of G6-OH PAMAM dendrimer was prepared from a 100.0 μM stock solution. To this, 55 equiv. of $CuSO_4$ were added from a 0.010 M stock solution. Aliquots of 0.30 M NaOH were added to adjust the pH to ~7.5, and this solution was stirred for 15 min to allow for Cu^{2+} complexation to the dendrimer. At this point, the

solution was purged with N_2, and it was kept under N_2 for the remainder of the synthetic procedure. Next, an equivalent (molar) amount of $NaBH_4$ was added from a freshly made 0.10 M stock solution. Reduction was allowed to proceed for at least 5 min.

Once reduction was complete, excess unreacted BH_4^- was oxidized by adding a four-fold excess (relative to the equiv. of BH_4^-) of 0.1 M $HClO_4$ and allowing it to react for 5 min (the pH was maintained above 5 with NaOH throughout the synthesis). The pH of the solution was then raised to ~6.5 so that additional equiv. of Cu^{2+} could be complexed with the dendrimer. This cycle (adjust pH to > 6.5, add Cu^{2+}, wait for complexation, reduce, oxidize excess BH_4^-) was repeated as many times as necessary to synthesize Cu DENs of the desired size. At this stage, the pH was lowered to 3.2 and galvanic exchange for Pt was carried out by adding sufficient Pt^{2+} (from a freshly prepared 0.10 M stock solution of $PtCl_4^{2-}$) to the Cu DENs solution so that the Pt^{2+}:Cu ratio was 1. The resulting Pt DENs solution was immediately immobilized on Vulcan carbon using the procedures described in the next two sections.

Analysis by scanning transmission electron microscopy (STEM)

The G6-OH$(Pt^{2+})_n$ precursor, Pt DENs synthesized by chemical reduction, and Pt DENs synthesized by galvanic exchange (collectively referred to as Pt-dendrimer composites) were immobilized on Vulcan carbon by diluting a 2.0 µM solution of the Pt-dendrimer composite to 200 nM and then adding 2.0 mg of Vulcan carbon per mL of diluted Pt-dendrimer composite. This ratio of dendrimers:carbon ensured sufficient separation (for imaging purposes) between individual Pt-dendrimer composites on the surface of the Vulcan carbon. Isopropyl alcohol (final concentration: 20 vol%) was added to each solution to assist with dispersion of the carbon. The resulting ink was sonicated for 1 min, then 2.0 µL of this solution was pipetted onto a lacey-carbon-over-Ni transmission electron microscopy (TEM) grid (Electron Microscopy Sciences, Hatfield, PA), and finally the grid was dried in air. A JEOL JEM-ARM200F STEM with spherical aberration (Cs) correction and a high-angle annular dark-field (HAADF) detector was used for sample analysis.

Analysis by X-ray absorption spectroscopy (XAS)

As for the STEM analysis, the Pt-dendrimer composites were also immobilized on Vulcan carbon for XAS. The XAS analysis requires a higher surface concentration of the Pt-dendrimer composites, however, so 2.0 mg of Vulcan carbon per mL of the undiluted (2.0 μM) composite was used. The carbon-supported Pt-dendrimer composites were then filtered using an Advantec PTFE membrane filter (0.5 μm pore size). The filtrate was rinsed with water and then isopropyl alcohol, and allowed to dry in air overnight. The dried powder was pressed into a pellet at 1 ton of pressure for XAS analysis. XAS analysis was performed at the National Synchrotron Light Source at Brookhaven National Lab using beamline X18b. The data were collected in transmission mode using gas ionization detector chambers. A Pt foil was fit to obtain the amplitude factor (S_0^2 = 0.87 for the Pt L_3 edge was used). The data were analyzed using the IFFEFIT and Horae software packages.[60-62] The first shell was fit in R-space using a k-weight of 2 for the Fourier transforms.

Analysis by X-ray photoelectron spectroscopy (XPS)

A portion of the same pellet used for the XAS analysis was used for XPS. The pellet fragment was dissolved in water,

and an aliquot was pipetted onto a chip of glassy carbon. XPS was performed using a Kratos Axis Ultra spectrometer (Chestnut Ridge, NY) having an Al Kα source. Individual elemental spectra were collected with a 0.1 eV step size and a band pass energy of 20 eV. Binding energies were calibrated against the C 1s line at 284.5 eV.[72] CasaXPS (version 2.3.15, Casa Software, Teignmouth, UK) was used for peak fitting, assuming a mixed Gaussian/Lorentzian model.

Results and Discussion

Synthesis of Pt DENs by chemical reduction

Before describing our new method for complete reduction of Pt DENs, we discuss the original BH_4^--reduction method, which leads to only partial reduction, for comparison. The UV-vis spectra of the G6-OH$(Pt^{2+})_n$ (n = 55, 140, and 225) precursor before and after reduction with BH_4^- are provided in Figure 3.2. These spectra show that even after reduction with 50-fold excess BH_4^-, a fraction of the ligand-to-metal charge-transfer (LMCT) band of G6-OH$(Pt^{2+})_n$ (λ_{max} = 250 nm) and the absorbance bands arising from the unreduced Pt^{2+} salt (λ_{max} = 215 and 230 nm) are present. Consistent with previous findings, this indicates incomplete reduction of the G6-OH$(Pt^{2+})_n$ precursor.[27]

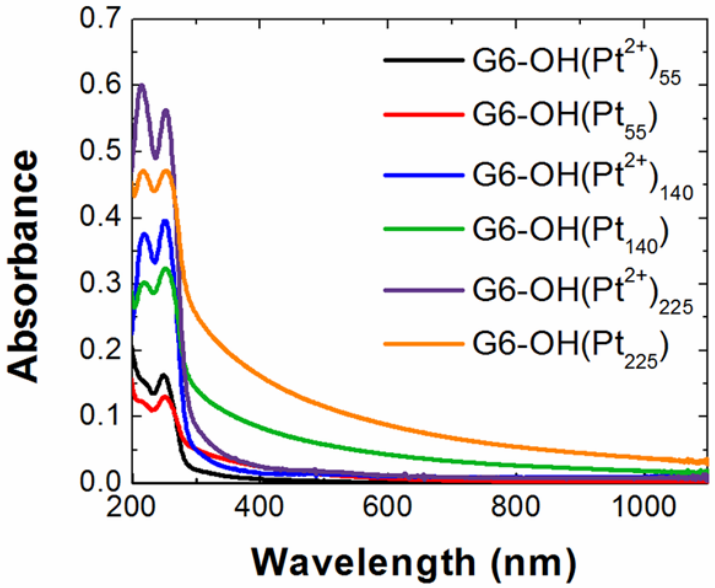

Figure 3.2

UV-vis spectra of Pt-dendrimer complexes, G6-OH$(Pt^{2+})_n$, and Pt DENs synthesized by BH_4^- reduction, G6-OH(Pt_n), where *n* = 55, 140, and 225. The spectra were acquired using a 2.0 mm quartz cuvette and blanked with 2.0 µM G6-OH.

Synthesis of Pt DENs by galvanic exchange

As discussed in the experimental section, Pt DENs prepared by galvanic exchange are synthesized by sequentially complexing and reducing aliquots of Cu^{2+} in the presence of G6-OH, and then reacting the resulting Cu DENs with Pt^{2+}. To prepare Cu DENs containing more than 64 atoms, multiple complexation and reduction steps are required. This is because, as we have previously shown, the maximum number of Cu^{2+} ions that can be complexed with the interior tertiary

amines of G6-OH is 64.[93] Accordingly, the Cu DEN synthesis begins by complexing a slightly substoichiometric amount of Cu^{2+} (55 equiv.) with G6-OH. As shown in Figure 3.3a, this results in a well-defined LMCT band at λ_{max} = 300 nm corresponding to the G6-OH$(Cu^{2+})_{55}$ precursor. Following reduction with BH_4^-, this LMCT band disappears and the characteristic broad absorbance of 55-atom Cu DENs is observed in Figure 3.3b.[93] After removal of excess BH_4^- by addition of $HClO_4$, 55 additional equiv. of Cu^{2+} are added to the solution and the LMCT band is observed again (Figure 3.3a), but now it is superimposed on the spectrum of the reduced G6-OH(Cu_{55}) DENs. Importantly, the appearance of the LMCT band confirms that no active BH_4^- is present in solution, because the added Cu^{2+} is still in its oxidized form and able to complex to the dendrimer (at pH > 6.5). After the second aliquot of Cu^{2+} is sequestered inside the dendrimer, additional BH_4^- is added to yield reduced DENs containing an average of 110 atoms: G6-OH(Cu_{110}). As shown in Figure 3.3b this results in an increase in the featureless absorbance spanning the indicated wavelength range. This process is then continued until Cu DENs of the desired size are formed. In this case, we stopped the process at 140 total equiv. of Cu in order to make a direct comparison to BH_4^--reduced Pt DENs of the same nominal

size (140 is a complete-shell magic number for a truncated octahedron nanoparticle).

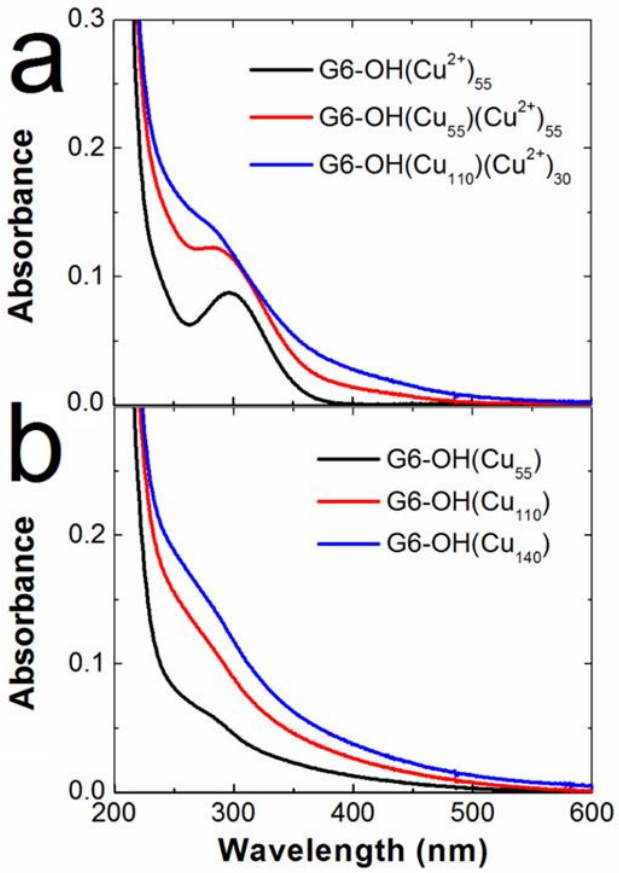

Figure 3.3

(a) UV-vis spectra for each sequential complexation step of the synthesis of G6-OH(Cu_{140}) DENs. (b) UV-vis spectra for each sequential reduction step in the synthesis of G6-OH(Cu_{140}) DENs.

The Cu DENs are converted into Pt DENs by adding the same number of equiv. of $PtCl_4^{2-}$ as were used to prepare the Cu DENs. As previously reported for the synthesis of G6-

OH(Pt_{55}), this galvanic exchange reaction is carried out at pH ~3,[70] with the value here being 3.2. Figure 3.4 compares UV-vis spectra of the 140-atom Cu DENs at pH > 6.5 and the Pt DENs immediately after galvanic exchange (pH 3.2). Consistent with previous reports, the absorbance of the G6-OH(Pt_{140}) DENs is significantly higher than that of the corresponding Cu DENs.[70] Additionally, the Cu-LMCT band (λ_{max} = 300 nm) is absent after galvanic exchange at pH 3.2, because the interior tertiary amines of the dendrimer are protonated and hence not available for complexation with Cu^{2+}.[70] For direct comparison with the G6-OH(Cu_{140}) spectrum, the pH of the G6-OH(Pt_{140}) solution was then raised above 6.5. In this case, the pH is high enough that the interior tertiary amines can complex free Cu^{2+}, and a Cu-LMCT band is again apparent. This confirms that galvanic exchange has occurred and that Cu^{2+} is present in the solution.

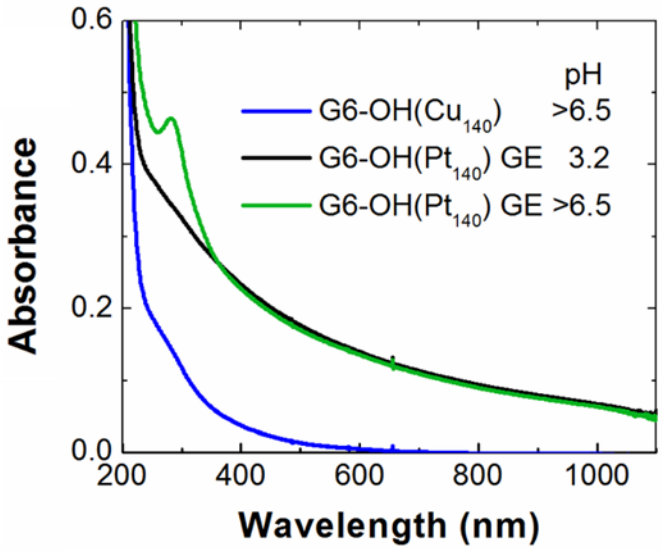

Figure 3.4

Comparison of the UV-vis spectra of G6-OH(Cu_{140}) prepared by direct reduction with BH_4^- (blue), and G6-OH(Pt_{140}) prepared by galvanic exchange at pH 3.2 (black) and at pH >6.5 (green). The concentration of the dendrimers in these solutions was 2.0 µM, and the data were obtained using a 2.00 mm quartz cuvette and blanked with water.

Pt DENs larger than *n*=140 can also be made by galvanic exchange. For example, Figure 3.5 compares G6-OH(Pt_{140}) and G6-OH(Pt_{225}) DENs. The abosrbance of G6-OH(Pt_{225}) is higher at all wavelengths, qualitatively indicating the presence of larger nanoparticles.

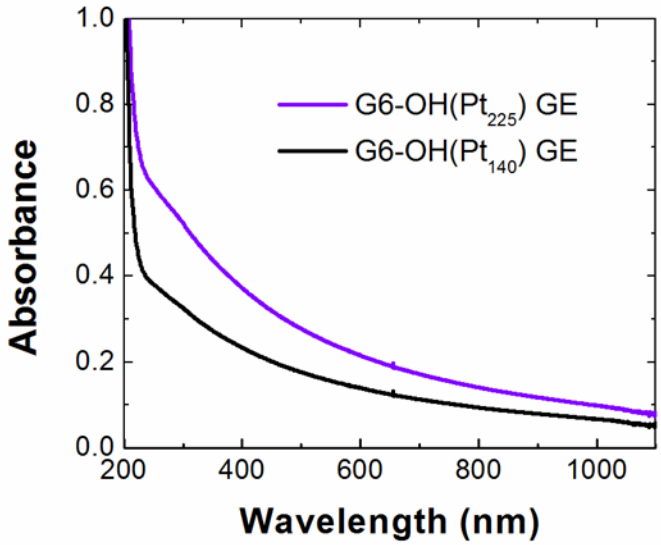

Figure 3.5

UV-vis spectra G6-OH(Pt_{140}) and G6-OH(Pt_{225}) DENs prepared by galvanic exchange (GE). As the size of the DENs increases, the absorption at all wavelengths does as well. These spectra were obtained at pH 3.2 using a 2.0 mm cuvette blanked with water.

Following synthesis, the Pt DENs were immobilized on Vulcan carbon, which as we have shown previously is a good support for performing electrocatalytic experiments using DENs.[38,58] Immobilization was carried out at pH 3.2 by the addition of Vulcan carbon and subsequent filtration as described in the experimental section. TEM images and size-distribution histograms of G6-OH(Pt_{140}) and G6-OH(Pt_{225}) immobilized on Vulcan, prepared using the aforementioned procedure, are shown in Figure 3.6. Consistent with

expectations, these data indicate that the DENs have diameters of 1.7 ± 0.2 nm for G6-OH(Pt_{140}) (calculated diameter = 1.6 nm) and 1.9 ± 0.2 nm for G6-OH(Pt_{225}) (calculated diameter = 1.9 nm).[84]

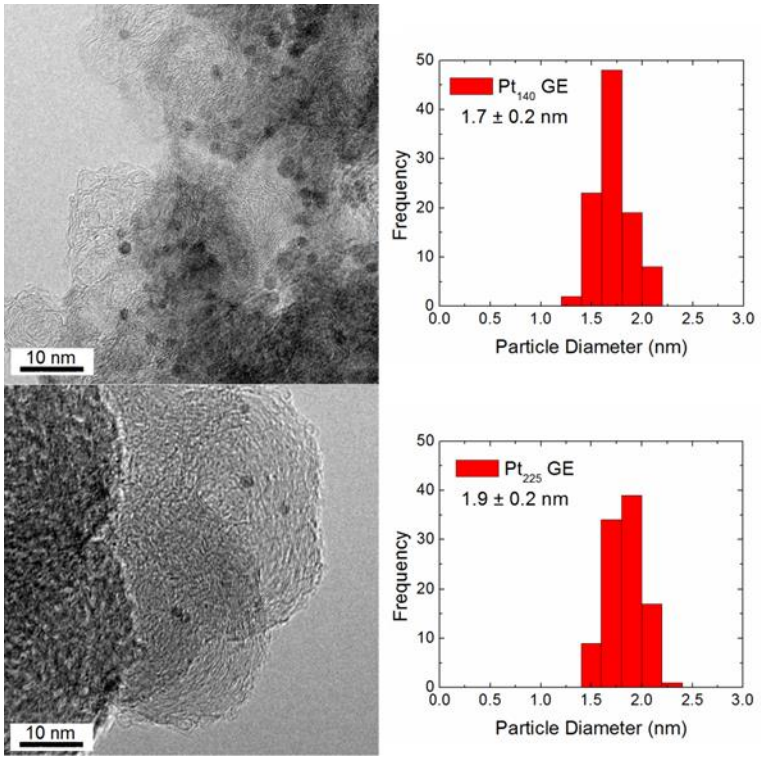

Figure 3.6

TEM images and corresponding size-distribution histograms for G6-OH(Pt_{140})(top) and G6-OH(Pt_{225}) (bottom) DENs synthesized by galvanic exchange. Transmission electron microscopy (TEM) images were obtained using a JEOL-2010F TEM operating at 200 kV.

STEM results

The conclusion that a bimodal distribution of fully reduced and unreduced DENs results from the standard BH_4^- reduction method relies in part on results from a previous TEM study. In that earlier analysis, micrographs showed that direct reduction resulted in Pt DENs having the expected size distribution despite other analytical methods indicating incomplete reduction.[27] At that time, however, we did not have access to electron microscopy with sufficient resolution and contrast to image the G6-OH$(Pt^{2+})_n$ precursor. Now, by utilizing high-resolution aberration-corrected STEM, individual Pt atoms/ions are visible, and hence it is possible to distinguish between the G6-OH$(Pt^{2+})_n$ precursor and G6-OH(Pt_n) DENs. The STEM data discussed next confirm that BH_4^- reduction results in a bimodal distribution of reduced and unreduced DENs.

Figure 3.7a is a STEM micrograph of the G6-OH$(Pt^{2+})_{55}$ precursor that has not been exposed to BH_4^-. This image shows clusters of individual Pt atoms/ions on the Vulcan carbon surface. To highlight the nature of these groupings, red circles having diameters of ~7 nm (the approximate diameter of G6 PAMAM dendrimers)[94] have been overlaid onto the image. Although highly qualitative, it is not difficult to imagine that these clusters of atoms/ions are contained within

individual dendrimers. The micrograph in Figure 3.7b was obtained after direct BH_4^- reduction of the G6-OH$(Pt^{2+})_{55}$ precursor. In this case, both ordered nanoparticles (~1.3 nm,[27] indicated by red arrows) and a grouping of atoms (red circle) are visible on the Vulcan carbon support. This observation is consistent with the partial (bimodal) reduction model. Specifically, the approximate spread of the disordered atoms is maintained at ~7 nm, suggesting that some of the complexes are unaffected by the chemical reduction process.

Figure 3.7c shows that G6-OH(Pt_{55}) DENs synthesized by galvanic exchange of Cu for Pt reveal no sign of the unreduced G6-OH$(Pt^{2+})_{55}$ complex (that is, no evidence of individual atoms were apparent despite extensive analysis of the grid). Rather, only fully reduced particles were observed. This same trend is observed for G6-OH$(Pt^{2+})_{140}$, G6-OH(Pt_{140}) prepared by BH_4^- reduction, and G6-OH(Pt_{140}) prepared by galvanic exchange (Figure 3.7d, Figure 3.7e, and Figure 3.7f, respectively) and for G6-OH$(Pt^{2+})_{225}$ and G6-OH(Pt_{225}) prepared by BH_4^- reduction (Figure 3.7g and Figure 3.7h, respectively). In summary, the representative micrographs shown in Figure 3.7 confirm, qualitatively, our earlier bimodal-distribution model, wherein a fraction of the G6-OH$(Pt^{2+})_n$ species remain unreduced when exposed to BH_4^-, while the remainder are reduced to yield

G6-OH(Pt_n) DENs.[27] In contrast, galvanic exchange results in complete reduction. We wish to emphasize, however, that a much larger statistical analysis would be required to confirm these conclusions if they were solely based on electron microscopy. As discussed in the next three sections, however, spectroscopic evidence is conclusive.

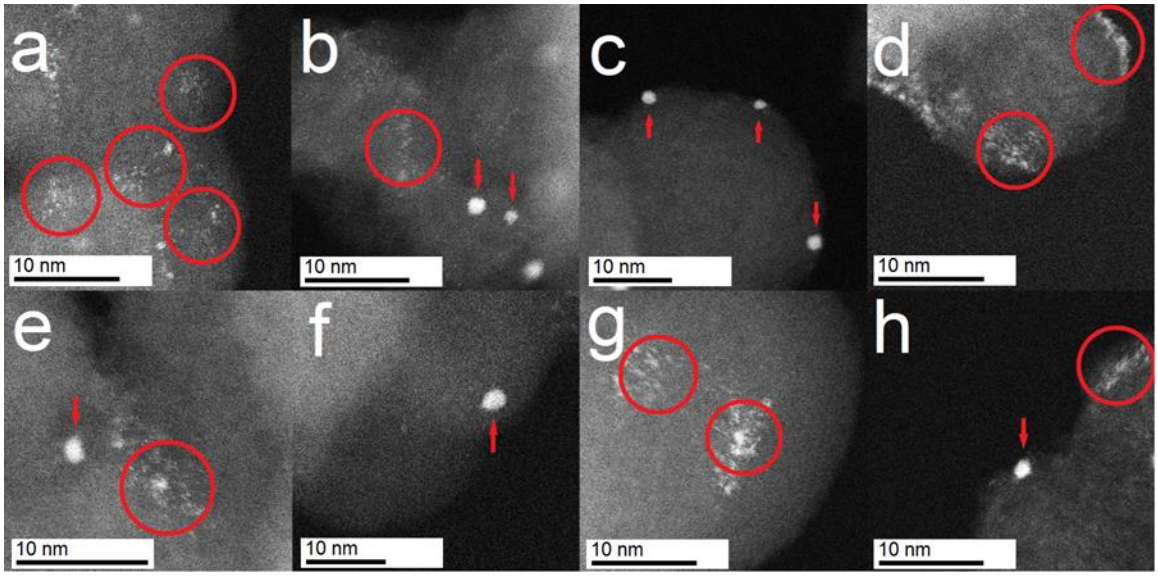

Figure 3.7

Representative STEM images of: (a) the G6-OH(Pt^{2+})$_{55}$ precursor complex, (b) G6-OH(Pt_{55}) synthesized by direct reduction with BH_4^-, (c) G6-OH(Pt_{55}) synthesized by galvanic exchange, (d) the G6-OH(Pt^{2+})$_{140}$ precursor complex, (e) G6-OH(Pt_{140}) synthesized by direct reduction with BH_4^-, (f) G6-OH(Pt_{140}) synthesized by galvanic exchange, (g) the G6-OH(Pt^{2+})$_{225}$ precursor complex, and (h) G6-OH(Pt_{225}) synthesized by direct reduction with BH_4^-. The red circles (~7 nm in diameter) represent the approximate width of a G6 PAMAM dendrimer, and highlight the groupings of atoms present in the precursor complex or with incomplete reduction by BH_4^-. The red arrows mark the presence of reduced DENs.

XPS analysis

Although it is difficult to obtain quantitative information about the extent of Pt DEN reduction from TEM studies, XPS is very well suited for this purpose. Accordingly, we used XPS to compare the extent of reduction using the BH_4^- and galvanic exchange approaches. As shown in Figure 3.8a, the Pt $4f_{7/2}$ peaks for G6-OH$(Pt^{2+})_n$ (n = 55, 140, and 225) are present at 72.9, 73.3, and 73.5 eV, respectively. These values can be compared with that of the $PtCl_4^{2-}$ starting material: 73.4 eV (black vertical line).[72] The slight shift to lower binding energy as the Pt:dendrimer ratio decreases may result from the increased availability of dendrimer binding sites at lower Pt^{2+} concentrations and the corresponding increase in multidentate binding.[88,91]

The spectrum of the BH_4^--reduced DENs (G6-OH(Pt_n), n = 55, 140, and 225) exhibit multiple pairs of peaks, which is consistent with partial reduction and two populations of Pt oxidation states. Focusing on the Pt $4f_{7/2}$ region, the peaks at ~71.8 ± 0.2 eV correspond to zerovalent DENs. The black vertical line at 71.3 eV marks the value previously reported for the $4f_{7/2}$ peak for Pt DENs.[27] In addition to these zerovalent Pt 4f peaks, a second set of 4f peaks, corresponding to the G6-OH$(Pt^{2+})_n$ precursor, are also present. These results are consistent with our previous finding that

the BH_4^- method leads to only partial reduction of the precursor.[27]

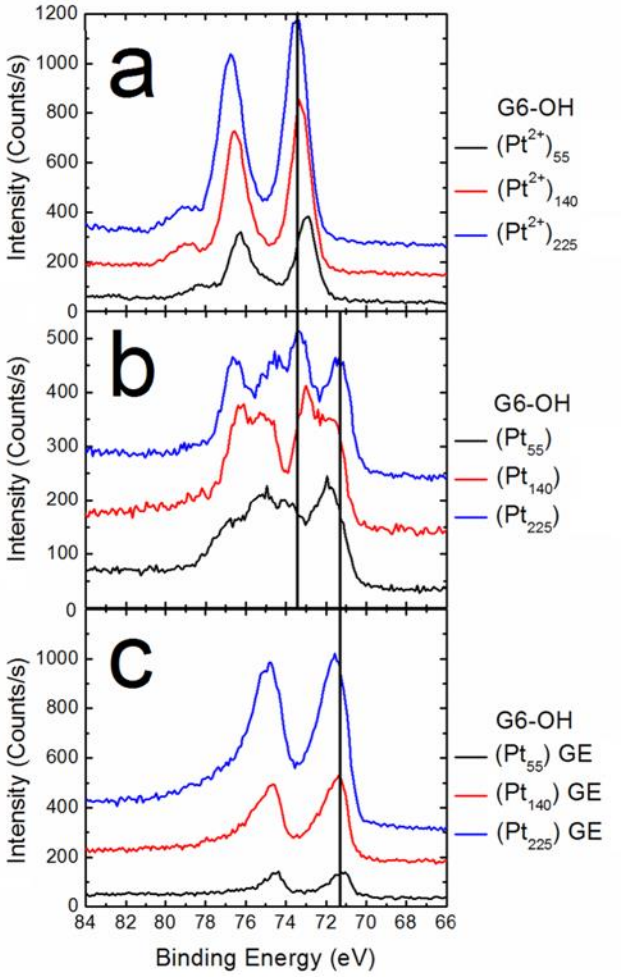

Figure 3.8

High-resolution XPS spectra of (a) G6-OH$(Pt^{2+})_n$, (b) G6-OH(Pt_n) synthesized by direct reduction with BH_4^-, and (c) G6-OH(Pt_n) synthesized by galvanic exchange (GE), where *n* = 55, 140, and 225. The vertical black lines at 73.4 eV and 71.3 eV represent literature values for the binding energies of $PtCl_4^{2-}$ and fully reduced Pt DENs, respectively.

The XPS peaks in Figure 3.8b were fit to quantify the extent of reduction for each sample. The fits are shown in Figure 3.9 and quantitative results are provided in Table 3.1.

	Percent Reduction	
	XPS	XANES
G6-OH(Pt55)	59%	54%
G6-OH(Pt140)	40%	42%
G6-OH(Pt225)	43%	50%

Table 3.1

Percentage reduction of Pt DENs synthesized by direct BH_4^- reduction.

In all cases, the total XPS spectra are well represented by deconvolution into peaks corresponding to the Pt^0 and Pt^{2+} binding energies. The extent of reduction determined from these fits is 59%, 40%, and 43% for G6-OH(Pt_n) (*n* = 55, 140, and 225) DENs, respectively. These values are somewhat different than those we have reported previously for *n* = 55, 147, and 240: 14%, 44%, and 64%, respectively.[27] We attribute the large difference in the percent reduction of G6-OH(Pt_{55}) to the larger excess of BH_4^- used for reduction in the present set of experiments (50-fold versus 10-fold).

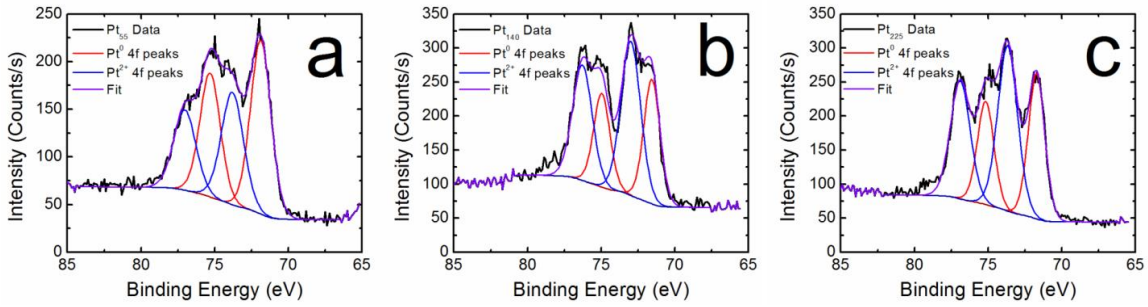

Figure 3.9

Fits of (a) Pt_{55}, (b) Pt_{140}, and (c) Pt_{225} DENs reduced using BH_4^-. The data were fit using a combination of Pt^0 (red) and Pt^{2+} (blue) 4f peaks. CasaXPS (version 2.3.15, Casa Software, Teignmouth, UK) was used for peak fitting, assuming a mixed Gaussian/Lorentzian model.

Figure 3.8c shows XPS spectra of the G6-OH(Pt_n) DENs prepared by galvanic exchange. In contrast to the spectra of the BH_4^--reduced DENs in Figure 3.8b, these spectra exhibit just one $4f_{7/2}$ peak corresponding to fully reduced Pt. These results indicate that complete galvanic exchange has occurred with the Cu DENs and that little or no unreduced Pt salt or complex is present in the sample.

XANES analysis

XANES linear combination analysis (LCA) was used to further quantify the extent of Pt reduction and to verify the XPS results. Figure 3.10a shows that the white line intensity

of the G6-OH(Pt_{55}) DENs prepared by direct BH_4^- reduction is between that of the corresponding G6-OH(Pt^{2+})$_{55}$ precursor and G6-OH(Pt_{55}) DENs synthesized by galvanic exchange. The spectrum of G6-OH(Pt_{55}) prepared by direct reduction and the fit obtained from a linear combination of the G6-OH(Pt^{2+})$_{55}$ precursor and G6-OH(Pt_{55}) prepared by galvanic exchange are shown in Figure 3.10b. The overlap is nearly exact, and it indicates a percentage reduction of the precursor of 59%, which compares favorably with the value of 54% determined by XPS (Table 3.1).

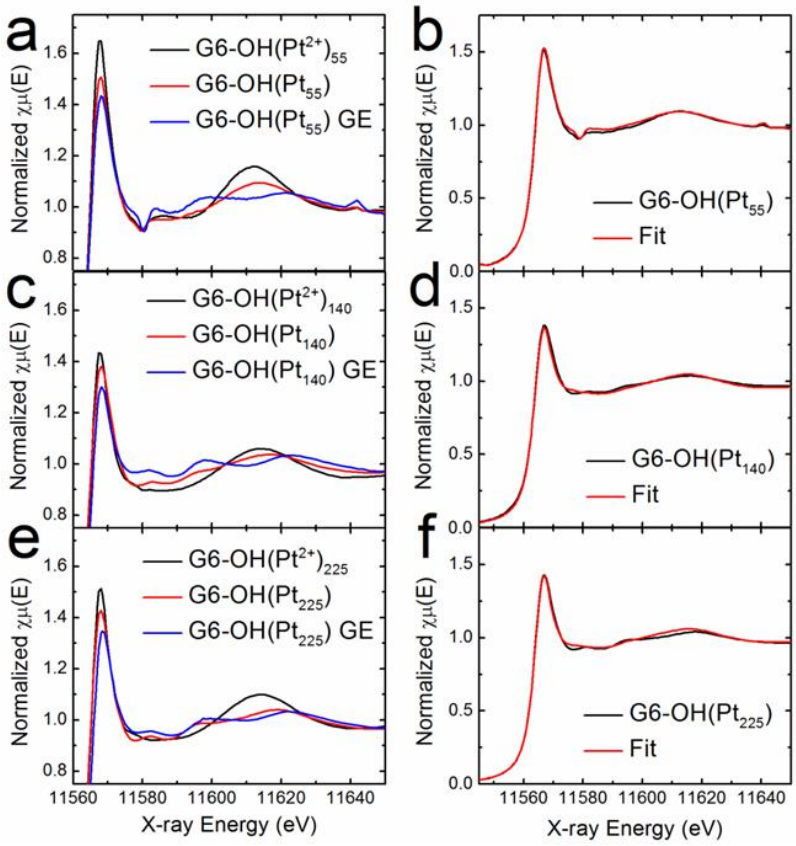

Figure 3.10

XANES data (left) and LCA fits (right) for: (a,b) G6-OH(Pt_{55}), (c,d) G6-OH(Pt_{140}), and (e,f) G6-OH(Pt_{225}). For the right panel, the data corresponding to the DENs synthesized by BH_4^- reduction are shown in black and the LCA best fit is in red.

XANES spectra for the *n* = 140 and 225 DENs and DEN precursors are shown in Figure 3.10c and Figure 3.10e, respectively. The corresponding LCA fitting for the G6-OH(Pt_{140}) and G6-OH(Pt_{225}) DENs (direct BH_4^- reduction) in Figure 3.10d and Figure 3.10f, respectively, provide good matches.

The resulting percentage reductions of the precursors are within 7% of those determined by XPS (Table 3.1).

EXAFS analysis

EXAFS spectra were acquired to obtain the coordination number for the fully reduced G6-OH(Pt_n) DENs synthesized by galvanic exchange. Figure 3.11 shows the R-space data and corresponding fits. The fits yield coordination numbers of 8.9 ± 1.2 for G6-OH(Pt_{140}) and 9.2 ± 1.2 for G6-OH(Pt_{225}). These values can be compared to those calculated for 140-atom and 225-atom truncated octahedra of 9.09 and 9.49, respectively.[95] These values are substantially higher than those reported previously for Pt DENs reduced with BH_4^-: 3.99 ± 0.61 for G6-OH(Pt_{147}) and 6.09 ± 0.42 for G6-OH(Pt_{240}).[27] The latter very low coordination numbers indicate the presence of a substantial number of unreduced Pt species, which is consistent with the previously discussed XANES and XPS results. An important outcome of the EXAFS analysis is that in the future it will be possible to use in situ electrochemical EXAFS to study electrocatalysis at fully reduced Pt DENs.

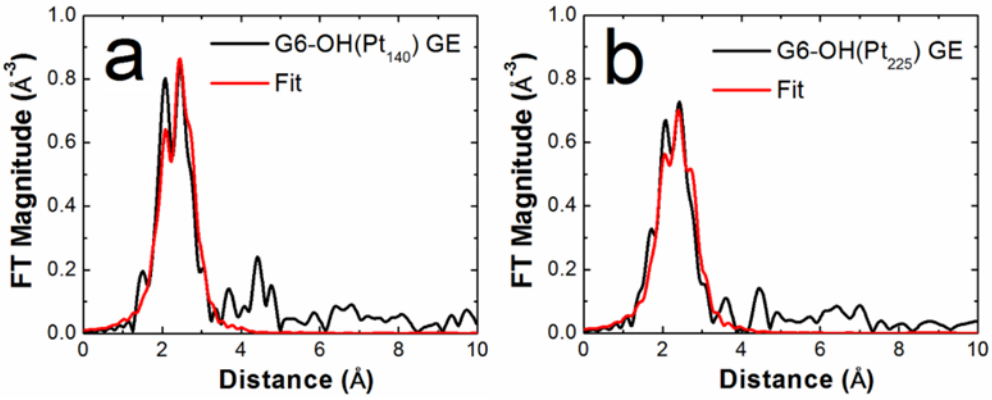

Figure 3.11

EXAFS data (black) and R-space fits (red) (k-weight of 2) for Pt DENs prepared by galvanic exchange.

Summary and Conclusions

A general scheme for synthesizing fully reduced Pt DENs has been described. The synthesis is carried out by first preparing Cu DENs of the desired size, and then using the process of galvanic exchange to convert these into Pt DENs containing the same number of atoms. We also re-examined the originally reported method for preparing Pt DENs by direct reduction using BH_4^-,[27] and confirmed that this approach leads to a bimodal distribution of fully reduced DENs and fully unreduced precursors.

The present research focus of our group is reconciling the experimentally measured and theoretically calculated electrocatalytic properties of DENs. Due to their high

activity for many catalytic reactions, Pt DENs are among the most important materials for developing this type of structure-activity relationship. The types of future studies we envision require, to the maximum extent possible, homogeneity in catalyst size and structure, and the results reported here move us a step closer to this goal.

Chapter 4: A Theoretical and Experimental In situ Electrochemical Infrared Spectroscopy Study of Adsorbed CO on Pt Dendrimer-Encapsulated Nanoparticles

Introduction

We are interested in developing a better understanding of how small changes in the structure of nanoparticles in the 1-2 nm size range affect the electrocatalytic properties of important reactions like oxygen reduction and CO oxidation. We approach this problem by directly comparing theory and experiments.[96] This is important because previous results from our group and others have shown that nanoparticle structures in this size range are dynamic. For example, core@shell nanoparticles are able to invert,[37,80] ligands can drive shape changes,[79] and interactions with a substrate can result in major electronic and shape changes.[76,97,98]

One effective method for gaining insight into nanoparticle surface structure is to measure changes in the vibrational frequency of adsorbed CO (CO_{ads}) using infrared (IR) spectroscopy.[99,100] Spectroscopic results from single-crystal surface models are relevant for understanding the structure of Pt nanoparticles (PtNPs) having size >4 nm, but for smaller nanoparticles the connection to bulk surfaces is

more tenuous.[99] This is because with smaller nanoparticles the dominance of discrete facets is reduced, while the contribution of edge and corner sites increases. These latter sites can be identified because they bind CO more strongly, thereby decreasing its stretching frequencies.[99,101]

It has previously been shown that the CO_{ads} frequency decreases as the size of PtNPs supported on carbon (C/PtNP) decreases.[99,102,103] For example, frequency shifts on the order of 20 cm^{-1} have been reported as nanoparticle size decreases from ~4 nm to ~2 nm.[99] However, these studies were carried out with commercial C/PtNP catalysts, which exhibit wide variations in the size and shape of the PtNPs and also effects exerted by the support.[103,104] This in turn makes it difficult to precisely correlate IR spectra to particular nanoparticle structures.

We sought to better understand the interaction between CO and PtNPs by developing a more refined model system that could be directly compared to first principles theory. The model we chose are dendrimer-encapsulated nanoparticles (DENs), which are well-defined materials in the size range of 1-2 nm.[22,96] DENs are synthesized by first complexing metal ions to the interior of the dendrimer, and then adding a reducing agent. This results in nearly monodisperse nanoparticles that are sterically trapped within the

dendrimer interior. The size of DENs can be tuned by changing the ratio of metal ions:dendrimer. Another advantage of DENs is that the dendrimer protects the nanoparticles from agglomeration, but it only weakly interacts with the surface.[105] Additionally, the presence of the dendrimer prevents direct contact between the catalyst and the electrode surface, thereby eliminating contributions to the shape or electronic properties of the nanoparticle arising from support interactions. Note, however, that the slight separation between DENs and the electrode surface does not adversely impact electrocatalytic rate measurements.[106,107] Finally, DENs can be attached to electrodes without using Vulcan carbon or Nafion, both of which are in common use and can influence the structural, spectroscopic, and electrochemical properties of nanoparticles.[108-110] For all these reasons, DENs simplify direct comparison of theory and experiment.

In addition to its use as a reporter of nanoparticle structure,[99,111] the binding energy of CO_{ads} is of interest as a descriptor for different catalytic reactions such as CO electrooxidation, formic acid oxidation, and methanol oxidation.[58,112-115] In the size range of DENs, the corresponding structure can be modeled using density functional theory (DFT)

to make predictions about structure and the binding energies of adsorbates.[96]

In the present study, we report in situ electrochemical IR spectroscopy and cyclic voltammetry (CV) measurements of CO_{ads} on Pt DENs containing an average of 147 atoms (Pt_{147}),[22] and then compare these experimental results to DFT calculations. The key observation is that the frequency of the CO_{ads} stretching mode is shifted by ~8 cm^{-1} to lower values on Pt_{147} DENs as compared to a bulk Pt(111) single crystal. The corresponding DFT calculations are consistent with this finding. Importantly, the magnitude of this shift is significantly smaller than that previously reported for commercial supported C/PtNPs. We believe the difference between the results obtained using the DENs model and these earlier studies is due to the absence of support effects, a narrower particle-size distribution, and the absence of ligand effects caused Nafion or other binders.

Experimental Section

Chemicals

Sixth-generation, hydroxyl-terminated (G6-OH) poly(amidoamine) (PAMAM) dendrimers in methanol were purchased from Dendritech (Midland, MI). The dendrimer

solvent was removed under vacuum, and then the dendrimers were reconstituted in water at a concentration of 100.0 μM. $NaBH_4$ and K_2PtCl_4 were purchased from Sigma-Aldrich, and $CuSO_4$, NaOH and high-purity $HClO_4$ from Fisher Scientific. All solutions were made using deionized (DI) water having a resistivity of 18.2 MΩ•cm (Milli-Q gradient system, Millipore).

Synthesis and characterization of Pt DENs synthesized by galvanic exchange

The synthesis of Pt DENs by galvanic exchange has been previously reported.[70,92] Briefly,[116] a 10.0 μM solution of G6-OH PAMAM dendrimer was prepared by dilution of a 100.0 μM stock solution. Next, 55 equiv. of $CuSO_4$ were added from a 0.10 M stock solution. The pH was adjusted to ~7.5 using 0.30 M NaOH, and then the solution was purged with N_2 and stirred for at least 5 min to allow for complexation between Cu^{2+} and the dendrimer. The solution was continuously purged with N_2 for the remainder of the synthesis procedure. An equivalent amount of $NaBH_4$ as $CuSO_4$ was then added from a freshly prepared 0.10 M stock solution, and the solution stirred for at least 5 min.

Excess unreacted BH_4^- was oxidized by adding a four-fold excess (relative to the original equiv. of BH_4^-) of 0.1 M $HClO_4$

and allowing it to react for 5 min (the pH was maintained above 5 with NaOH throughout the synthesis). The pH of the solution was then raised to ~6.5 so that additional equiv. of Cu^{2+} could be complexed with the dendrimer. This complexation/reduction cycle was repeated twice more to synthesize Cu_{147} DENs (first with 55 equiv. then with 37 equiv.). The pH was lowered to 3.2 and galvanic exchange for Pt was carried out by adding 147 equiv. of Pt^{2+} (from a freshly prepared 0.10 M stock solution of $PtCl_4^{2-}$) to the Cu DENs solution so that the Pt^{2+}:Cu ratio was 1. After reacting for several minutes the N_2 purge was stopped and the pH of the resulting Pt DENs solution was raised to ~8.5. An aliquot of the DENs solution was diluted to 2.0 μM, and ~3 μL was pipetted onto a ultra-thin carbon-over-Cu transmission electron microscopy (TEM) grid (Electron Microscopy Sciences, Hatfield, PA), and the grid was allowed to dry in air. A JEOL-2010F TEM operating at 200 kV was used for size analysis of the Pt DENs.

Electrochemistry

CVs were obtained in a 0.10 M $HClO_4$ electrolyte solution using a 3 mm glassy carbon (GC) disk electrode, a Au counter electrode, and a Hg/Hg_2SO_4 reference electrode (CH

Instruments, Austin, Texas), which was calibrated against an eDAQ Hydroflex hydrogen reference electrode. All potentials were converted to, and reported relative to, the reversible hydrogen electrode (RHE) scale. For electrochemical measurements, a CHI 1202B potentiostat (CH Instruments) was used. For CVs the electrolyte solution was purged with either high-purity Ar or CO.

Electrochemical immobilization of DENs

The GC disk electrode was polished with alumina, rinsed, and then sonicated for ~2 min in DI water. Next, Pt DENs were immobilized on the GC disk electrode using a previously reported electrochemical procedure.[25] The DEN concentration used for immobilization was 5.0 μM, and three full potential cycles were performed between 0.50 and 1.30 V. After immobilization, the electrode was rinsed with DI water, and then the DEN surfaces were cleaned by cycling the potential 20 times between 0 and 1.3 V in 0.10 M $HClO_4$.

In situ IR spectroscopy

For IR measurements, a ~1 cm x 1 cm GC chip electrode was used. A Cu wire was attached to the backside with conductive Ag paint, and then the entire back and edges of

the GC chip were covered with epoxy (to prevent Ag or Cu contamination). The Cu wire was threaded through a glass rod to provide stability in the electrochemical cell. Electrochemical immobilization of DENs and subsequent cleaning cycles were carried out for the GC chip electrode as previously described for the GC disk electrode. The Teflon spectroelectrochemical cell[117] was filled with CO-saturated 0.10 M $HClO_4$ and outfitted with a Pt counter electrode and a saturated calomel electrode. The GC chip working electrode was positioned and secured firmly against the top of a hemispherical ZnSe attenuated total reflectance (ATR) crystal (at the bottom of the cell). A potential of 0.05 V was applied, the spectroelectrochemical cell lid closed, and the entire compartment housing the spectroelectrochemical cell and detector was closed and purged with dry compressed air for ~1 h.

IR spectra were obtained using a Nicolet 6700 FTIR having an MCT-A liquid nitrogen-cooled detector. A spectrum of CO_{ads} was obtained at 0.05 V immediately after purging the system with dry air. Next the potential was stepped to 0.96 V to oxidize and desorb CO_{ads}, and then a reference spectrum was obtained. Both spectra were acquired at 8 cm^{-1} resolution and 1024 scans were co-added. The two single-beam reflectivities were subtracted and normalized to isolate the signal due to

the CO_{ads} using the following equation: $-\Delta R/R = -(R - R_{ref})/R_{ref})$. Here, R is the reflectivity in the presence of CO_{ads}, and R_{ref} is the reference spectrum collected in the absence of CO_{ads}. The spectrum of CO_{ads} on Pt_{147} DENs is plotted as $\Delta R/R$ to correct for the peak inversion observed with respect to the Pt(111) electrode. Peak inversion has been previously reported for thin noble metal catalyst layers on GC electrodes.[118,119]

In addition to Pt DENs, spectra of CO_{ads} were also obtained from a Pt(111) single crystal. The crystal was prepared by heating for 10 min and then allowing it to cool in an Ar-purged tube. The electrode was then immediately placed into the in situ IR set up, and then the same procedure used for the Pt_{147} DENs was followed for IR experiments.

Computational methods

DFT calculations were performed using the Vienna ab initio simulation package.[65,66] Core electrons were described using the projector-augmented wave method.[68,69] Kohn-Sham single-electron wave functions were expanded in a plane-wave basis with a kinetic energy cutoff of 280 eV to describe the valence electrons. The generalized gradient approximation (GGA) using the Perdew-Wang 91 functional was chosen to evaluate the exchange-correlation energy.[67] All atoms in the

nanoparticle were allowed to relax; geometries were considered optimized when the force on each atom was <0.005 eV/Å. Convergence was checked by increasing the energy cut-off to 400 eV, and the CO binding energy on a Pt 147-atom nanoparticle was found to change by only 1 meV (<0.1%). Theoretical IR spectra were calculated based on the fully optimized structures using Porezag's scheme as implemented in the Atomic Simulation Environment (ASE).[120]

Pt_{147} was modeled as a 147-atom face-centered cubic (fcc) cuboctahedron nanoparticle in a 3 nm cubic cell, which ensures a sufficient vacuum gap between periodic images. The Pt(111) surface was modeled as a (4×4) Pt(111) slab with 4 atomic layers and 14 Å of vacuum. The Brillouin zone was sampled using a 4×4×1 Monkhorst-Pack k-point mesh for Pt(111) and the Gamma point for Pt_{147}.[121]

Results and Discussion

Synthesis and immobilization of Pt_{147} DENs

Pt_{147} DENs were prepared as follows. First, as described in detail in the Experimental Section, Cu_{147} DENs were prepared by sequential complexation and reduction steps. Second, the Cu_{147} DENs were reacted with Pt^{2+} to yield Pt_{147} DENs via a process known as galvanic exchange.[92,122] Figure 1 shows a TEM

micrograph of the resulting Pt_{147} DENs as well as a size-distribution histogram. The average diameter for Pt_{147} is 1.7 ± 0.2 nm, which is consistent with previous reports[27,84,116] and with the calculated diameter of 1.6 nm.[84] The close proximity of the DENs in Figure 1a suggests some interaction between the dendrimers upon drying on the carbon TEM grid, but these DENs are stable in solution and exhibit no evidence of agglomeration. Note that the diameter of each DEN was measured by assuming each to be a separate, spherical nanoparticle.

The Pt_{147} DENs were immobilized onto a GC disk electrode using a previously reported electrochemical immobilization method[25] that is briefly summarized in the Experimental Section. Although surrounded by dendrimers and not in direct electrical contact with the underlying electrode, the Pt_{147} nanoparticles are in electrochemical equilibrium with the electrode surface.[106,107] The electrochemically active surface area of the Pt_{147} DENs was determined by integrating the hydride adsorption region of CVs and found to be 0.058 ± 0.005 cm^2. This corresponds to a coverage of ~1.7 monolayer of close-packed dendrimers, which is consistent with previous reports.[28,56] This calculation is approximate and relies on the diameter of the nanoparticles determined by TEM (1.7 nm) and several reasonable assumptions that we have outlined previously.[84]

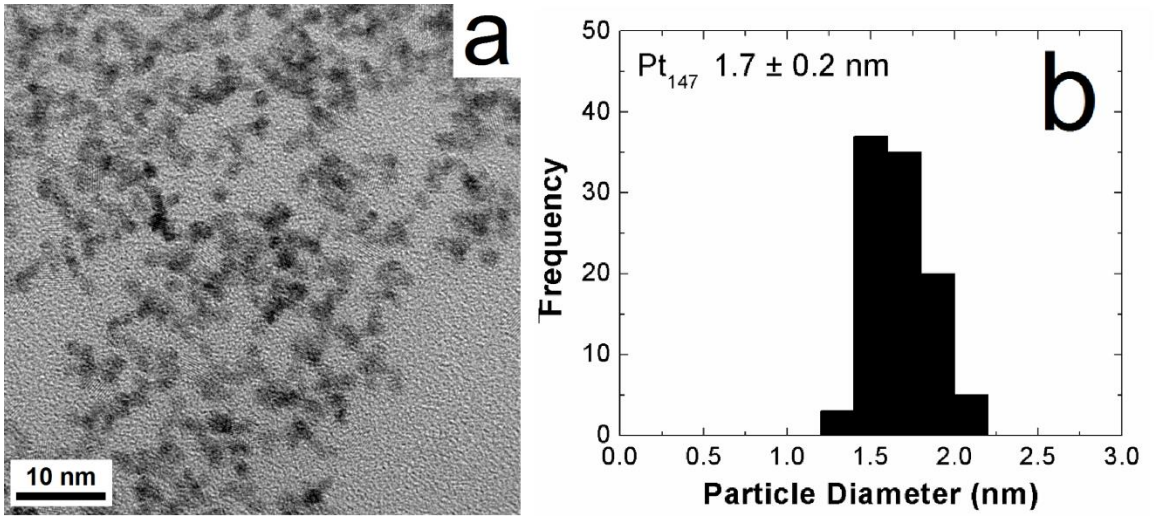

Figure 4.1

(a) TEM image of Pt_{147} DENs.(b) Size-distribution histogram of Pt_{147} DENs showing an average diameter of 1.7 ± 0.2 nm.

CO oxidation

Electrochemical experiments were performed to determine the CO stripping peak potential. The electrode was prepared as described in the Experimental Section, and then moved to a fresh solution of CO-purged 0.10 M $HClO_4$. Next, the potential was stepped to 0.05 V, and after 5 min the purge gas was changed to Ar for an additional 5 min. This results in adsorption of CO onto the Pt surface and removal of bulk CO from solution. As shown in Figure 2, the electrode potential was then cycled from 0.05 V to 1.30 V and then back to 0 V twice. Notice that the current axis in Figure 2 is

normalized to the electrochemically active surface area of Pt.

During the first positive-going scan, which begins at 0.050 V, CO_{ads} is oxidized to CO_2 at 0.92 ± 0.03 V. At higher potentials, the Pt_{147} DEN surface oxidizes, and upon scan reversal a PtO_x reduction peak is present at ~0.68 V. As the potential continues to decrease, the onset of hydride adsorption is observed at ~0.30 V on the now naked Pt surface. At the beginning of the second cycle, hydride desorption features are observed due to the absence of CO_{ads} but the characteristic CO_{ads} oxidation peak is not observed. The remainder of the second scan very nearly overlaps the first scan. The key point is that the procedure we developed to immobilize Pt_{147} DENs on the carbon electrode, saturate their surfaces with CO, and then remove CO_{ads} is effective. Accordingly, we are prepared to examine the CO_{ads} vibrational frequency using in situ IR spectroscopy.

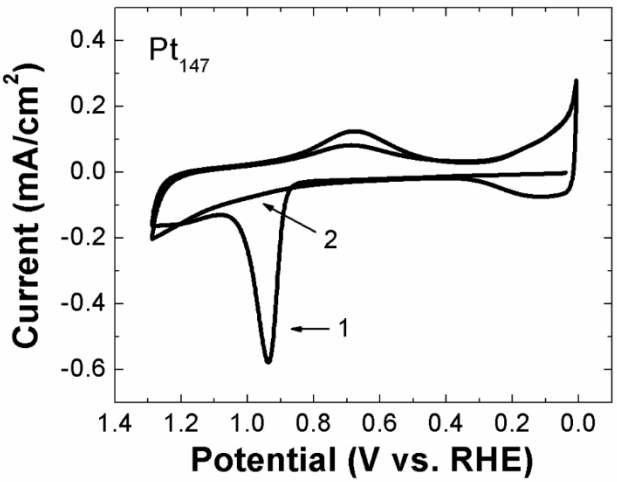

Figure 4.2

CV of Pt_{147} DENs showing the stripping of a monolayer of CO_{ads} in 0.1 M $HClO_4$. The scan rate was 50 mV/s, beginning at 0.05 V and in the positive direction. The currents reported are normalized to the electrochemically active Pt surface area.

In situ electrochemical IR

The technique of subtractively normalized interfacial Fourier transform infrared spectroscopy (SNIFTIRS) has been used extensively to study CO_{ads} on bulk (usually single crystal) metal surfaces,[36,123] but there are few reports of its use for understanding CO_{ads} on nanoparticles having sizes ≤ 2 nm.[99,100,102,103,124] Note, however, that in situ IR has been used to study CO_{ads} on DENs in the gas phase.[125]

To ensure that we are able to duplicate literature procedures and for comparative purposes, we first obtained a spectrum of CO_{ads} on a Pt(111) single crystal prepared as

described in the Experimental Section. The SNIFTERS spectrum was obtained as follows. First, a spectrum was obtained with the electrode potential was held at 0.050 V, where we would expect it to be covered with CO_{ads}. A second spectrum was then measured after stepping the potential to 0.96 V, where CO_{ads} is oxidized to soluble CO_2 and hence removed from the electrode surface. These two spectra were processed as described in the Experimental Section, and the result is shown in Figure 3a. The CO_{ads} stretching band is very strong, narrow, and centered at 2066 cm^{-1}. These features are characteristic of previously reported observations.[126-128]

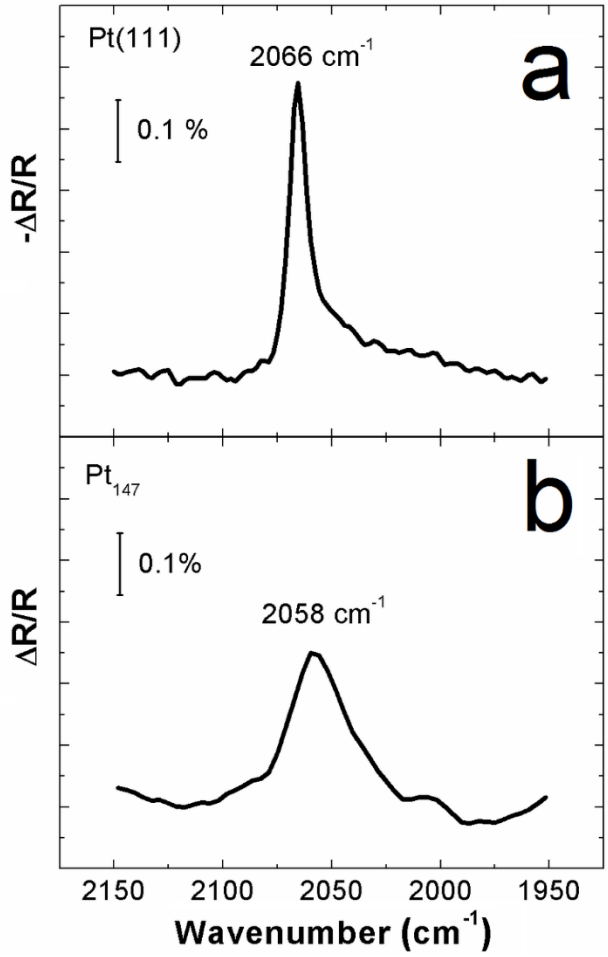

Figure 4.3

IR spectra of CO_{ads} on (a) Pt(111) and (b) Pt_{147} DENs. The spectrum of CO_{ads} was acquired at 0.05 V, and a reference spectrum (no CO_{ads}) was collected at 0.96 V. The electrolyte solution was 0.10 M $HClO_4$. A total of 1024 scans were collected at 8 cm^{-1} resolution.

Following the same procedure used for the Pt(111) single crystal, we next obtained an IR spectrum of CO_{ads} on the Pt_{147} DEN-modified GC electrode (Figure 3b). The resulting peak is broader, less intense, and shifted by 8

cm^{-1} to 2058 cm^{-1}. These features are similar to those previously reported for Pt_{147} DENs in an ethanol solution but not under potential control (CO_{ads} peak centered at 2063 cm^{-1}).[125]

The direction of the CO_{ads} peak shift between Pt(111) and Pt_{147} DENs (Figure 3) is in accord with prior literature reports of a redshift with decrease in size of nanoparticles <4 nm in diameter. However, its magnitude (8 cm^{-1}) is quite different. For example, Arenaz et al. observed a value of 2052 cm^{-1} for ~2.0-2.5 nm C/PtNPs and 2049 cm^{-1} for ~1-1.5 nm C/PtNPs (shifts of 14 and 17 cm^{-1}, respectively, compared to Pt(111)) using the same applied electrode potential and a Nafion binding layer.[102] Park et al. observed a value of ~2042 cm^{-1} (a shift of 24 cm^{-1} compared to Pt(111)) for 2.0 nm C/PtNPs (the size distribution was not specified) using an applied potential of 0 V.[99] The difference in the magnitude of these reported shifts and that represented in Figure 3 is most likely a consequence of support interactions present in the earlier studies. In contrast, DENs are unsupported nanoparticles in the sense that there is no direct contact between the DENs and the electrode surface. Previous nuclear magnetic resonance (NMR) reports have investigated the effect the interaction between the conductive carbon support and PtNPs has on the CO_{ads} frequency.[103,104] A stronger electronic

effect was observed on smaller nanoparticles, and suggested that shifts in frequency with size are dominated by this strong support interaction.[103] DENs are not subject to such strong interactions, and this could be an explanation for why a smaller shift is observed here.

DFT calculations

DFT was used in order to understand more about the observed IR frequency shift between Pt(111) and Pt_{147}. The Pt(111) system was first investigated. A monolayer of CO in the atop binding configuration was used to generate the IR spectrum for Pt(111) in Figure 4 (black trace). The coverage of CO on Pt(111), however, has been previously experimentally determined to be 0.75.[127] Figure 5 shows the dependence of the average CO frequency with coverage, and between a full monolayer coverage and 0.75 monolayer coverage, a shift of ~20 cm^{-1} occurs. As such, the calculated value (2072 cm^{-1}) is shifted by this 20 cm^{-1} to yield a value of 2052 cm^{-1} for Pt(111). Next, the Pt_{147} model was constructed. A monolayer of atop CO was added to the Pt_{147} structure and the CO stretching frequencies computed. Here, a monolayer of CO is consistent with the experimental data. The reason that Pt_{147} can accommodate more CO as compared to Pt(111) is that the high

fraction of edge and corner sites, set by the high curvature of the NP surface, reduces CO-CO repulsion.

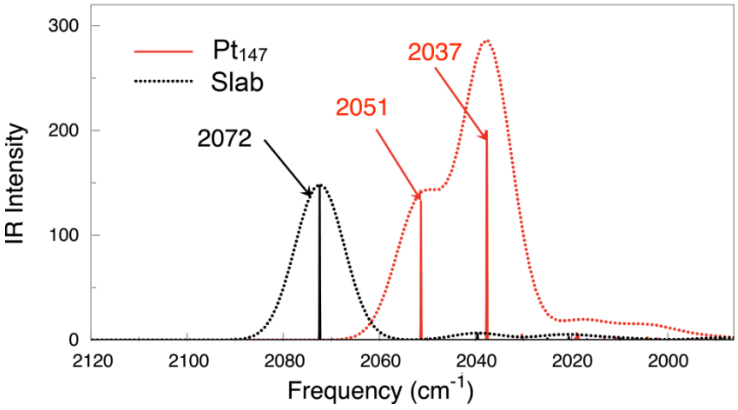

Figure 4.4

Calculated vibrational spectra of CO_{ads} on Pt(111) and Pt_{147} DENs.

Figure 4 (red trace) shows the calculated IR spectrum, with two main populations centered at 2051 cm^{-1} and 2037 cm^{-1} with an average value of 2049 cm^{-1}. The peak splitting is due to coupling between the CO molecules resulting in in-phase and out-of-phase CO stretching modes across the entire NP. One important difference to note between experiment and theory is that the applied electrochemical potential is not taken into account in the DFT calculations, so we are only interested in comparing shifts and not absolute frequency values. To correlate experiment and theory, we begin by looking at the observed experimental shift between the Pt(111)

and Pt_{147} system. Experimentally, this was found to be 8 cm^{-1}. This is close in magnitude to the difference of ~11 cm^{-1} observed between the Pt(111) and the Pt_{147} theoretical spectra. The broadening of the experimental Pt_{147} IR peak as compared to the single crystal Pt(111) peak is also seen in the theoretical spectra, but with the 8 cm^{-1} resolution used here it is difficult to interpret more from the shape of the experimental peaks. From the agreement seen here between experiment and theory in the direction and magnitude of the shift between Pt DENs and the Pt(111) crystal, our model system of the Pt_{147} DEN is corroborated. As this is a complicated electrochemical system involving potential control and other factors, it is valuable to know that relative shifts observed theoretically for important reactant descriptors (such as CO_{ads}) are valid for application to experimental systems.

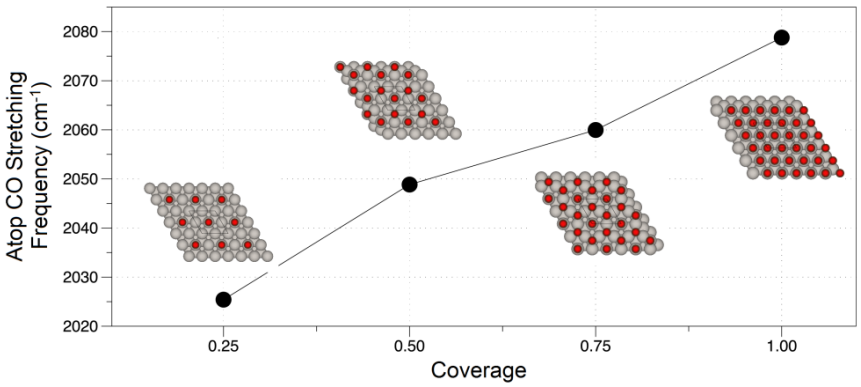

Figure 4.5

Plot of the calculated trend of frequency of atop CO_{ads} vs. the fractional coverage on a Pt(111) surface.

Summary and Conclusions

We have presented a combined experimental and theoretical study of CO_{ads} on Pt_{147} DENs. IR spectroscopy revealed an 8 cm^{-1} redshift of the CO_{ads} stretching frequency on Pt_{147} DENs in relation to a Pt(111) crystal, which is in agreement with the calculated shift from the theoretical model systems. This shift is significantly smaller than has been previously observed in the literature, which we attribute to lack of support effects and the narrow size distribution of DENs. The agreement found between experiment and theory validates the model nanoparticle system used. This will allow for the use for CO-binding as a probe for future bimetallic structural studies, and as a descriptor of catalytic activity

on DENs for reactions such as formic acid oxidation and methanol oxidation.

Chapter 5: Conclusions and Outlook

In this dissertation, the structural and catalytic activity of DENs has been investigated with the goal of providing an improved model system for strengthening the connection between experiment and theory of metallic nanoparticles. Unusual structural characteristics were observed, in particular in the Pd@Pt core@shell system which underwent inversion to form a Pt@Pd structure. This case study highlights the importance of fully characterizing the model system before drawing conclusions about catalytic activity measurements. Incorrect assumptions of nanoparticle structure can be detrimental to the validation process of theoretical models.

Another theme presented in this work is that theory can be used not only to make predictions of relative activity, but also to learn more about the model system. By doing segregation energy studies on the Pd@Pt system it was possible to gain understanding about the mechanism of inversion. This joining of experiment and theory is what makes these model systems so powerful. By using model nanoparticles in the size range accessible to high-level calculations, both experiment and theory gain understanding.

The Pt DENs system is also presented in this dissertation. The synthesis through galvanic exchange for Cu

DENs yields fully reduced Pt DEN catalysts. This synthetic procedure provides an improved model system that is no longer complicated by incomplete reduction of the Pt salt. This simplifies the interpretation of characterization results as well as the comparison to theory. The system of Pt_{147} was then studied using IR spectroscopy with adsorbed CO as a probe, and a corresponding theoretical model investigated. This fundamental study can be applied in future studies to more complicated reaction mechanisms. The electrooxidation of formic acid and methanol are two examples of more complex reactions in which the binding of CO plays a role. The in situ IR experimental set-up provides a platform for directly studying the CO_{ads} frequency with comparison to theory, which can be related to binding energy and used a predictor of activity. This can be used not only with the Pt DENs system, but also core@shell motifs such as Au@Pt. Au@Pt DENs have been previously shown to have enhanced formic acid oxidation activity. The expansion of the DENs system to more complicated reaction systems is one future direction of this work.

References

1. Goodman, D. W. Model Catalytic Studies over Metal Single Crystals. *Acc. Chem. Res.* **1984**, *17*, 194-200.

2. Chang, S. C.; Weaver, M. J. In Situ Infrared Spectroscopy at Single-Crystal Metal Electrodes: an Emerging Link Between Electrochemical and Ultrahigh-Vacuum Surface Science. *J. Phys. Chem.* **1991**, *95*, 5391-5400.

3. Herrero, E.; Buller, L. J.; Abruña, H. D. Underpotential Deposition at Single Crystal Surfaces of Au, Pt, Ag and Other Materials. *Chem. Rev.* **2001**, *101*, 1897-1930.

4. Sachtler, J. W. A.; Somorjai, G. A. Influence of ensemble size on CO chemisorption and catalytic n-hexane conversion by Au-Pt(111) bimetallic single-crystal surfaces. *J. Catal.* **1983**, *81*, 77-94.

5. Zhou, W.-P.; Yang, X.; Vukmirovic, M. B.; Koel, B. E.; Jiao, J.; Peng, G.; Mavrikakis, M.; Adzic, R. R. Improving Electrocatalysts for O_2 Reduction by Fine-Tuning the Pt–Support Interaction: Pt Monolayer on the Surfaces of a $Pd_3Fe(111)$ Single-Crystal Alloy. *J. Am. Chem. Soc.* **2009**, *131*, 12755-12762.

6. Taylor, C.; Kelly, R. G.; Neurock, M. Theoretical Analysis of the Nature of Hydrogen at the Electrochemical

Interface Between Water and a Ni(111) Single-Crystal Electrode. *J. Electrochem. Soc.* 2007, *154*, F55-F64.

7. Norskov, J. K.; Bligaard, T.; Rossmeisl, J.; Christensen, C. H. Towards the computational design of solid catalysts. *Nat Chem* 2009, *1*, 37-46.

8. Hernández, J.; Solla-Gullón, J.; Herrero, E.; Feliu, J. M.; Aldaz, A. In Situ Surface Characterization and Oxygen Reduction Reaction on Shape-Controlled Gold Nanoparticles. *J. Nanosci. Nanotechnol.* 2009, *9*, 2256-2273.

9. Nørskov, J. K.; Abild-Pedersen, F.; Studt, F.; Bligaard, T. Density functional theory in surface chemistry and catalysis. *Proc. Natl. Acad. Sci. U.S.A.* 2011, *108*, 937-943.

10. Nørskov, J. K.; Rossmeisl, J.; Logadottir, A.; Lindqvist, L.; Kitchin, J. R.; Bligaard, T.; Jónsson, H. Origin of the Overpotential for Oxygen Reduction at a Fuel-Cell Cathode. *J. Phys. Chem. B* 2004, *108*, 17886-17892.

11. Rossmeisl, J.; Logadottir, A.; Nørskov, J. K. Electrolysis of water on (oxidized) metal surfaces. *Chem. Phys.* 2005, *319*, 178-184.

12. Man, I. C.; Su, H.-Y.; Calle-Vallejo, F.; Hansen, H. A.; Martínez, J. I.; Inoglu, N. G.; Kitchin, J.; Jaramillo,

T. F.; Nørskov, J. K.; Rossmeisl, J. Universality in Oxygen Evolution Electrocatalysis on Oxide Surfaces. *ChemCatChem* 2011, *3*, 1159-1165.

13. Ferrin, P.; Nilekar, A. U.; Greeley, J.; Mavrikakis, M.; Rossmeisl, J. Reactivity descriptors for direct methanol fuel cell anode catalysts. *Surf. Sci.* 2008, *602*, 3424-3431.

14. Esposito, D. V.; Hunt, S. T.; Kimmel, Y. C.; Chen, J. G. A New Class of Electrocatalysts for Hydrogen Production from Water Electrolysis: Metal Monolayers Supported on Low-Cost Transition Metal Carbides. *J. Am. Chem. Soc.* 2012, *134*, 3025-3033.

15. Johnson, G. E.; Wang, C.; Priest, T.; Laskin, J. Monodisperse Au_{11} Clusters Prepared by Soft Landing of Mass Selected Ions. *Anal. Chem.* 2011, *83*, 8069-8072.

16. Oja, S. M.; Wood, M.; Zhang, B. Nanoscale Electrochemistry. *Anal. Chem.* 2013, *85*, 473-486.

17. Sambur, J. B.; Chen, P. Approaches to Single-Nanoparticle Catalysis. *Annu. Rev. Phys. Chem.* 2014, *65*, 395-422.

18. Crooks, R. M.; Zhao, M.; Sun, L.; Chechik, V.; Yeung, L. K. Dendrimer-Encapsulated Metal Nanoparticles: Synthesis, Characterization, and Applications to Catalysis. *Acc. Chem. Res.* 2001, *34*, 181-190.

19. Niu, Y.; Crooks, R. M. Dendrimer-encapsulated metal nanoparticles and their applications to catalysis. *C. R. Chim.* 2003, *6*, 1049-1059.

20. Scott, R. W. J.; Wilson, O. M.; Crooks, R. M. Synthesis, Characterization, and Applications of Dendrimer-Encapsulated Nanoparticles. *J. Phys. Chem. B* 2005, *109*, 692-704.

21. Bronstein, L. M.; Shifrina, Z. B. Dendrimers As Encapsulating, Stabilizing, or Directing Agents for Inorganic Nanoparticles. *Chem. Rev.* 2011, *111*, 5301-5344.

22. Myers, V. S.; Weir, M. G.; Carino, E. V.; Yancey, D. F.; Pande, S.; Crooks, R. M. Dendrimer-Encapsulated Nanoparticles: New Synthetic and Characterization Methods and Catalytic Applications. *Chem. Sci.* 2011, *2*, 1632-1646.

23. Zheng, J.; Petty, J. T.; Dickson, R. M. High Quantum Yield Blue Emission from Water-Soluble Au_8 Nanodots. *J. Am. Chem. Soc.* 2003, *125*, 7780-7781.

24. Bao, Y.; Zhong, C.; Vu, D. M.; Temirov, J. P.; Dyer, R. B.; Martinez, J. S. Nanoparticle-Free Synthesis of Fluorescent Gold Nanoclusters at Physiological Temperature. *J. Phys. Chem. C* 2007, *111*, 12194-12198.

25. Ye, H.; Crooks, R. M. Electrocatalytic O_2 Reduction at Glassy Carbon Electrodes Modified with Dendrimer-Encapsulated Pt Nanoparticles. *J. Am. Chem. Soc.* 2005, *127*, 4930-4934.

26. Petkov, V.; Bedford, N.; Knecht, M. R.; Weir, M. G.; Crooks, R. M.; Tang, W.; Henkelman, G.; Frenkel, A. Periodicity and Atomic Ordering in Nanosized Particles of Crystals. *J. Phys. Chem. C* 2008, *112*, 8907-8911.

27. Knecht, M. R.; Weir, M. G.; Myers, V. S.; Pyrz, W. D.; Ye, H.; Petkov, V.; Buttrey, D. J.; Frenkel, A. I.; Crooks, R. M. Synthesis and Characterization of Pt Dendrimer-Encapsulated Nanoparticles: Effect of the Template on Nanoparticle Formation. *Chem. Mater.* 2008, *20*, 5218-5228.

28. Yancey, D. F.; Carino, E. V.; Crooks, R. M. Electrochemical Synthesis and Electrocatalytic Properties of Au@Pt Dendrimer-Encapsulated Nanoparticles. *J. Am. Chem. Soc.* 2010, *132*, 10988-10989.

29. Zhang, L.; Iyyamperumal, R.; Yancey, D. F.; Crooks, R. M.; Henkelman, G. Design of Pt-Shell Nanoparticles with Alloy Cores for the Oxygen Reduction Reaction. *ACS Nano* 2013, *7*, 9168-9172.

30. Frenkel, A. Solving the 3D structure of metal nanoparticles. *Z. Kristallogr.* 2007, *222*, 605-611.

31. Frenkel, A. I. Applications of extended X-ray absorption fine-structure spectroscopy to studies of bimetallic nanoparticle catalysts. *Chem. Soc. Rev.* 2012, *41*, 8163-8178.

32. Frenkel, A. I.; Yevick, A.; Cooper, C.; Vasic, R. Modeling the Structure and Composition of Nanoparticles by Extended X-Ray Absorption Fine-Structure Spectroscopy. *Annu. Rev. Anal. Chem.* 2011, *4*, 23-39.

33. Bunker, G. *Introduction to XAFS*. Cambridge University Press: New York, 2010.

34. Zaera, F. New advances in the use of infrared absorption spectroscopy for the characterization of heterogeneous catalytic reactions. *Chem. Soc. Rev.* 2014, *43*, 7624-7663.

35. Marković, N. M.; Ross Jr, P. N. Surface science studies of model fuel cell electrocatalysts. *Surf. Sci. Rep.* 2002, *45*, 117-229.

36. Korzeniewski, C. Infrared Spectroscopy in Electrochemistry: New Methods and Connections to UhV Surface Science. *Crit. Rev. Anal. Chem.* 1997, *27*, 81-102.

37. Weir, M. G.; Knecht, M. R.; Frenkel, A. I.; Crooks, R. M. Structural Analysis of PdAu Dendrimer-Encapsulated Bimetallic Nanoparticles. *Langmuir* 2010, *26*, 1137-1146.

38. Yancey, D. F.; Zhang, L.; Crooks, R. M.; Henkelman, G. Au@Pt Dendrimer Encapsulated Nanoparticles As Model Electrocatalysts for Comparison of Experiment and Theory. *Chem. Sci.* 2012, *3*, 1033-1040.

39. Taufany, F.; Pan, C.-J.; Rick, J.; Chou, H.-L.; Tsai, M.-C.; Hwang, B.-J.; Liu, D.-G.; Lee, J.-F.; Tang, M.-T.; Lee, Y.-C.; Chen, C.-I. Kinetically Controlled Autocatalytic Chemical Process for Bulk Production of Bimetallic Core–Shell Structured Nanoparticles. *ACS Nano* 2011, *5*, 9370-9381.

40. Wang, J. X.; Inada, H.; Wu, L.; Zhu, Y.; Choi, Y.; Liu, P.; Zhou, W.-P.; Adzic, R. R. Oxygen Reduction on Well-Defined Core–Shell Nanocatalysts: Particle Size, Facet, and Pt Shell Thickness Effects. *J. Am. Chem. Soc.* 2009, *131*, 17298-17302.

41. Sanchez, S. I.; Small, M. W.; Zuo, J.-m.; Nuzzo, R. G. Structural Characterization of Pt–Pd and Pd–Pt Core–Shell Nanoclusters at Atomic Resolution. *J. Am. Chem. Soc.* 2009, *131*, 8683-8689.

42. Zhang, J.; Mo, Y.; Vukmirovic, M. B.; Klie, R.; Sasaki, K.; Adzic, R. R. Platinum Monolayer Electrocatalysts for O_2 Reduction: Pt Monolayer on Pd(111) and on Carbon-Supported Pd Nanoparticles. *J. Phys. Chem. B* 2004, *108*, 10955-10964.

43. Tessier, B. C.; Russell, A. E.; Theobald, B. R.; Thompsett, D. PtML/Pd/C Core-Shell Electrocatalysts for the ORR in PEMFCs. *ECS Trans.* 2009, *16*, 1-11.

44. Wang, Y.; Toshima, N. Preparation of Pd–Pt Bimetallic Colloids with Controllable Core/Shell Structures. *J. Phys. Chem. B* 1997, *101*, 5301-5306.

45. Li, G.; Lu, W.; Luo, Y.; Xia, M.; Chai, C.; Wang, X. Synthesis and Characterization of Dendrimer-Encapsulated Bimetallic Core-Shell PdPt Nanoparticles. *Chin. J. Chem.* 2012, *30*, 541-546.

46. Frenkel, A. I.; Wang, Q.; Sanchez, S. I.; Small, M. W.; Nuzzo, R. G. Short Range Order in Bimetallic Nanoalloys: An Extended X-ray Absorption Fine Structure Study. *J. Chem. Phys.* 2013, *138*, 064202.

47. Wells, P. P.; Crabb, E. M.; King, C. R.; Wiltshire, R.; Billsborrow, B.; Thompsett, D.; Russell, A. E. Preparation, Structure, and Stability of Pt and Pd Monolayer Modified Pd and Pt Electrocatalysts. *Phys. Chem. Chem. Phys.* 2009, *11*, 5773-5781.

48. Christoffersen, E.; Liu, P.; Ruban, A.; Skriver, H. L.; Nørskov, J. K. Anode Materials for Low-Temperature Fuel Cells: A Density Functional Theory Study. *J. Catal.* 2001, *199*, 123-131.

49. Tan, T. L.; Wang, L.-L.; Johnson, D. D.; Bai, K. A Comprehensive Search for Stable Pt–Pd Nanoalloy Configurations and Their Use As Tunable Catalysts. *Nano Lett.* 2012, *12*, 4875-4880.

50. Hansen, P. L.; Molenbroek, A. M.; Ruban, A. V. Alloy Formation and Surface Segregation in Zeolite-Supported Pt–Pd Bimetallic Catalysts. *J. Phys. Chem. B* 1997, *101*, 1861-1868.

51. Duan, Z.; Wang, G. Monte Carlo Simulation of Surface Segregation Phenomena in Extended and Nanoparticle Surfaces of Pt–Pd Alloys. *J. Phys.: Condens. Matter* 2011, *23*, 475301.

52. Huang, R.; Wen, Y.-H.; Zhu, Z.-Z.; Sun, S.-G. Pt–Pd Bimetallic Catalysts: Structural and Thermal Stabilities of Core–Shell and Alloyed Nanoparticles. *J. Phys. Chem. C* 2012, *116*, 8664-8671.

53. Wilson, O. M.; Knecht, M. R.; Garcia-Martinez, J. C.; Crooks, R. M. Effect of Pd Nanoparticle Size on the Catalytic Hydrogenation of Allyl Alcohol. *J. Am. Chem. Soc.* 2006, *128*, 4510-4511.

54. Myers, S. V.; Frenkel, A. I.; Crooks, R. M. X-ray Absorption Study of PdCu Bimetallic Alloy Nanoparticles Containing an Average of ~64 Atoms. *Chem. Mater.* 2009, *21*, 4824-4829.

55. Ye, H.; Crooks, R. M. Effect of Elemental Composition of PtPd Bimetallic Nanoparticles Containing an Average of 180 Atoms on the Kinetics of the Electrochemical Oxygen Reduction Reaction. *J. Am. Chem. Soc.* 2007, *129*, 3627-3633.

56. Carino, E. V.; Crooks, R. M. Characterization of Pt@Cu Core@Shell Dendrimer-Encapsulated Nanoparticles Synthesized by Cu Underpotential Deposition. *Langmuir* 2011, *27*, 4227-4235.

57. Carino, E. V.; Kim, H. Y.; Henkelman, G.; Crooks, R. M. Site-Selective Cu Deposition on Pt Dendrimer-Encapsulated Nanoparticles: Correlation of Theory and Experiment. *J. Am. Chem. Soc.* 2012, *134*, 4153-4162.

58. Iyyamperumal, R.; Zhang, L.; Henkelman, G.; Crooks, R. M. Efficient Electrocatalytic Oxidation of Formic Acid Using Au@Pt Dendrimer-Encapsulated Nanoparticles. *J. Am. Chem. Soc.* 2013, *135*, 5521-5524.

59. Carino, E. V.; Knecht, M. R.; Crooks, R. M. Quantitative Analysis of the Stability of Pd Dendrimer-Encapsulated Nanoparticles. *Langmuir* 2009, *25*, 10279-10284.

60. Newville, M. IFEFFIT: Interactive XAFS Analysis and FEFF Fitting. *J. Synchrotron Radiat.* 2001, *8*, 322-324.

61. Ravel, B.; Newville, M. ATHENA, ARTEMIS, HEPHAESTUS: Data Analysis for X-ray Absorption Spectroscopy Using IFEFFIT. *J. Synchrotron Radiat.* 2005, *12*, 537-541.

62. Ravel, B. ATOMS: Crystallography for the X-ray Absorption Spectroscopist. *J. Synchrotron Radiat.* 2001, *8*, 314-316.

63. Zabinsky, S. I.; Rehr, J. J.; Ankudinov, A.; Albers, R. C.; Eller, M. J. Multiple-Scattering Calculations of X-ray-Absorption Spectra. *Phys. Rev. B* 1995, *52*, 2995-3009.

64. Frenkel, A. I. Applications of Extended X-ray Absorption Fine-Structure Spectroscopy to Studies of Bimetallic Nanoparticle Catalysts. *Chem. Soc. Rev.* 2012.

65. Kresse, G.; Hafner, J. First-Principles Study of the Adsorption of Atomic H on Ni (111), (100) and (110). *Surf. Sci.* 2000, *459*, 287-302.

66. Kresse, G. Dissociation and Sticking of H_2 on the Ni(111), (100), and (110) Substrate. *Phys. Rev. B* 2000, *62*, 8295-8305.

67. Perdew, J. P.; Wang, Y. Accurate and Simple Analytic Representation of the Electron-Gas Correlation Energy. *Phys. Rev. B* 1992, *45*, 13244-13249.

68. Blöchl, P. E. Projector Augmented-Wave Method. *Phys. Rev. B* 1994, *50*, 17953-17979.

69. Kresse, G.; Joubert, D. From Ultrasoft Pseudopotentials to the Projector Augmented-Wave Method. *Phys. Rev. B* **1999**, *59*, 1758-1775.

70. Pande, S.; Weir, M. G.; Zaccheo, B. A.; Crooks, R. M. Synthesis, Characterization, and Electrocatalysis using Pt and Pd Dendrimer-Encapsulated Nanoparticles Prepared by Galvanic Exchange. *New J. Chem.* **2011**, *35*, 2054-2060.

71. Leff, D. V.; Ohara, P. C.; Heath, J. R.; Gelbart, W. M. Thermodynamic Control of Gold Nanocrystal Size: Experiment and Theory. *J. Phys. Chem.* **1995**, *99*, 7036-7041.

72. NIST X-ray Photoelectron Spectroscopy Database, Version 4.1 (National Institute of Standards and Technology, Gaithersburg, 2012); http://srdata.nist.gov/xps/.

73. Rose, A.; Maniguet, S.; Mathew, R. J.; Slater, C.; Yao, J.; Russell, A. E. Hydride Phase Formation in Carbon Supported Palladium Nanoparticle Electrodes Investigated Using *In Situ* EXAFS and XRD. *Phys. Chem. Chem. Phys.* **2003**, *5*, 3220-3225.

74. Adzic, R. R.; Zhang, J.; Sasaki, K.; Vukmirovic, M. B.; Shao, M.; Wang, J. X.; Nilekar, A. U.; Mavrikakis, M.; Valerio, J. A.; Uribe, F. Platinum Monolayer Fuel Cell Electrocatalysts. *Top. Catal.* **2007**, *46*, 249-262.

75. Qian, H.; Zhu, M.; Wu, Z.; Jin, R. Quantum Sized Gold Nanoclusters with Atomic Precision. *Acc. Chem. Res.* 2012, *45*, 1470-1479.

76. Cuenya, B. R. Synthesis and catalytic properties of metal nanoparticles: Size, shape, support, composition, and oxidation state effects. *Thin Solid Films* 2010, *518*, 3127-3150.

77. Kim, B. H.; Hackett, M. J.; Park, J.; Hyeon, T. Synthesis, Characterization, and Application of Ultrasmall Nanoparticles. *Chem. Mater.* 2014, *26*, 59-71.

78. Li, N.; Zhao, P.; Astruc, D. Anisotropic Gold Nanoparticles: Synthesis, Properties, Applications, and Toxicity. *Angew. Chem. Int. Ed.* 2014, *53*, 1756-1789.

79. Yancey, D. F.; Chill, S. T.; Zhang, L.; Frenkel, A. I.; Henkelman, G.; Crooks, R. M. A Theoretical and Experimental Examination of Systematic Ligand-Induced Disorder in Au Dendrimer-Encapsulated Nanoparticles. *Chem. Sci.* 2013, *4*, 2912-2921.

80. Anderson, R. M.; Zhang, L.; Loussaert, J. A.; Frenkel, A. I.; Henkelman, G.; Crooks, R. M. An Experimental and Theoretical Investigation of the Inversion of Pd@Pt Core@Shell Dendrimer-Encapsulated Nanoparticles. *ACS Nano* 2013, *7*, 9345-9353.

81. Zhao, M.; Crooks, R. M. Homogeneous Hydrogenation Catalysis with Monodisperse, Dendrimer-Encapsulated Pd and Pt Nanoparticles. *Angew. Chem. Int. Ed.* 1999, *38*, 364-366.

82. Scott, R. W. J.; Datye, A. K.; Crooks, R. M. Bimetallic Palladium–Platinum Dendrimer-Encapsulated Catalysts. *J. Am. Chem. Soc.* 2003, *125*, 3708-3709.

83. Lang, H.; May, R. A.; Iversen, B. L.; Chandler, B. D. Dendrimer-Encapsulated Nanoparticle Precursors to Supported Platinum Catalysts. *J. Am. Chem. Soc.* 2003, *125*, 14832-14836.

84. Ye, H.; Crooks, J. A.; Crooks, R. M. Effect of Particle Size on the Kinetics of the Electrocatalytic Oxygen Reduction Reaction Catalyzed by Pt Dendrimer-Encapsulated Nanoparticles. *Langmuir* 2007, *23*, 11901-11906.

85. Myers, V. S.; Frenkel, A. I.; Crooks, R. M. In Situ Structural Characterization of Platinum Dendrimer-Encapsulated Oxygen Reduction Electrocatalysts. *Langmuir* 2012, *28*, 1596-1603.

86. Weir, M. G.; Myers, V. S.; Frenkel, A. I.; Crooks, R. M. In situ X-ray Absorption Analysis of ~1.8 nm Dendrimer-Encapsulated Pt Nanoparticles during Electrochemical CO Oxidation. *ChemPhysChem* 2010, *11*, 2942-2950.

87. Alexeev, O. S.; Siani, A.; Lafaye, G.; Williams, C. T.; Ploehn, H. J.; Amiridis, M. D. EXAFS Characterization of Dendrimer–Pt Nanocomposites Used for the Preparation of Pt/γ-Al_2O_3 Catalysts. *J. Phys. Chem. B* **2006**, *110*, 24903-24914.

88. Borodko, Y.; Thompson, C. M.; Huang, W.; Yildiz, H. B.; Frei, H.; Somorjai, G. A. Spectroscopic Study of Platinum and Rhodium Dendrimer (PAMAM G4OH) Compounds: Structure and Stability. *J. Phys. Chem. C* **2011**, *115*, 4757-4767.

89. Borodko, Y.; Ercius, P.; Pushkarev, V.; Thompson, C.; Somorjai, G. From Single Pt Atoms to Pt Nanocrystals: Photoreduction of Pt^{2+} Inside of a PAMAM Dendrimer. *J. Phys. Chem. Lett.* **2012**, *3*, 236-241.

90. Ozturk, O.; Black, T. J.; Perrine, K.; Pizzolato, K.; Williams, C. T.; Parsons, F. W.; Ratliff, J. S.; Gao, J.; Murphy, C. J.; Xie, H.; Ploehn, H. J.; Chen, D. A. Thermal Decomposition of Generation-4 Polyamidoamine Dendrimer Films: Decomposition Catalyzed by Dendrimer-Encapsulated Pt Particles. *Langmuir* **2005**, *21*, 3998-4006.

91. Pellechia, P. J.; Gao, J.; Gu, Y.; Ploehn, H. J.; Murphy, C. J. Platinum Ion Uptake by Dendrimers: An NMR and AFM Study. *Inorg. Chem.* **2004**, *43*, 1421-1428.

92. Zhao, M.; Crooks, R. M. Intradendrimer Exchange of Metal Nanoparticles. *Chem. Mater.* **1999**, *11*, 3379-3385.

93. Zhao, M.; Sun, L.; Crooks, R. M. Preparation of Cu Nanoclusters within Dendrimer Templates. *J. Am. Chem. Soc.* 1998, *120*, 4877-4878.

94. Jackson, C. L.; Chanzy, H. D.; Booy, F. P.; Drake, B. J.; Tomalia, D. A.; Bauer, B. J.; Amis, E. J. Visualization of Dendrimer Molecules by Transmission Electron Microscopy (TEM): Staining Methods and Cryo-TEM of Vitrified Solutions. *Macromolecules* 1998, *31*, 6259-6265.

95. Glasner, D.; Frenkel, A. I. Geometrical Characteristics of Regular Polyhedra: Application to EXAFS Studies of Nanoclusters. *AIP Conf. Proc.* 2007, *882*, 746-748.

96. Anderson, R. M.; Yancey, D. F.; Zhang, L.; Chill, S. T.; Henkelman, G.; Crooks, R. M. A Theoretical and Experimental Approach for Correlating Nanoparticle Structure and Electrocatalytic Activity. *Acc. Chem. Res.* 2015, *48*, 1351-1357.

97. Daniel, M.-C.; Astruc, D. Gold Nanoparticles: Assembly, Supramolecular Chemistry, Quantum-Size-Related Properties, and Applications toward Biology, Catalysis, and Nanotechnology. *Chem. Rev.* 2004, *104*, 293-346.

98. Schauermann, S.; Nilius, N.; Shaikhutdinov, S.; Freund, H.-J. Nanoparticles for Heterogeneous Catalysis: New

Mechanistic Insights. *Acc. Chem. Res.* 2013, *46*, 1673-1681.

99. Park, S.; Wasileski, S. A.; Weaver, M. J. Electrochemical Infrared Characterization of Carbon-Supported Platinum Nanoparticles: A Benchmark Structural Comparison with Single-Crystal Electrodes and High-Nuclearity Carbonyl Clusters. *J. Phys. Chem. B* 2001, *105*, 9719-9725.

100. Mayrhofer, K. J. J.; Arenz, M.; Blizanac, B. B.; Stamenkovic, V.; Ross, P. N.; Markovic, N. M. CO surface electrochemistry on Pt-nanoparticles: A selective review. *Electrochim. Acta* 2005, *50*, 5144-5154.

101. Kappers, M. J.; van der Maas, J. H. Correlation between CO frequency and Pt coordination number. A DRIFT study on supported Pt catalysts. *Catal. Lett.* 1991, *10*, 365-373.

102. Arenz, M.; Mayrhofer, K. J. J.; Stamenkovic, V.; Blizanac, B. B.; Tomoyuki, T.; Ross, P. N.; Markovic, N. M. The Effect of the Particle Size on the Kinetics of CO Electrooxidation on High Surface Area Pt Catalysts. *J. Am. Chem. Soc.* 2005, *127*, 6819-6829.

103. Rice, C.; Tong; Oldfield, E.; Wieckowski, A.; Hahn, F.; Gloaguen, F.; Léger, J.-M.; Lamy, C. In Situ Infrared Study of Carbon Monoxide Adsorbed onto Commercial Fuel-Cell-Grade Carbon-Supported Platinum Nanoparticles:

Correlation with ^{13}C NMR Results. *J. Phys. Chem. B* 2000, *104*, 5803-5807.

104. Tong; Rice, C.; Wieckowski, A.; Oldfield, E. A Detailed NMR-Based Model for CO on Pt Catalysts in an Electrochemical Environment: Shifts, Relaxation, Back-Bonding, and the Fermi-Level Local Density of States. *J. Am. Chem. Soc.* 2000, *122*, 1123-1129.

105. Gomez, M. V.; Guerra, J.; Velders, A. H.; Crooks, R. M. NMR Characterization of Fourth-Generation PAMAM Dendrimers in the Presence and Absence of Palladium Dendrimer-Encapsulated Nanoparticles. *J. Am. Chem. Soc.* 2009, *131*, 341-350.

106. Chazalviel, J.-N.; Allongue, P. On the Origin of the Efficient Nanoparticle Mediated Electron Transfer across a Self-Assembled Monolayer. *J. Am. Chem. Soc.* 2011, *133*, 762-764.

107. Barfidokht, A.; Ciampi, S.; Luais, E.; Darwish, N.; Gooding, J. J. Distance-Dependent Electron Transfer at Passivated Electrodes Decorated by Gold Nanoparticles. *Anal. Chem.* 2013, *85*, 1073-1080.

108. Sharma, S.; Pollet, B. G. Support materials for PEMFC and DMFC electrocatalysts—A review. *J. Power Sources* 2012, *208*, 96-119.

109. McGovern, M. S.; Garnett, E. C.; Rice, C.; Masel, R. I.; Wieckowski, A. Effects of Nafion as a binding agent for unsupported nanoparticle catalysts. *J. Power Sources* 2003, *115*, 35-39.

110. Malevich, D.; Li, J.; Chung, M. K.; McLaughlin, C.; Schlaf, M.; Lipkowski, J. In situ IR reflectance absorption spectroscopy studies of the effect of Nafion on CO adsorption and electrooxidation at Pt nanoparticles. *J. Solid State Electrochem.* 2005, *9*, 267-276.

111. Gumeci, C.; Marathe, A.; Behrens, R. L.; Chaudhuri, J.; Korzeniewski, C. Solvothermal Synthesis and Electrochemical Characterization of Shape-Controlled Pt Nanocrystals. *J. Phys. Chem. C* 2014, *118*, 14433-14440.

112. Lee, S. W.; Chen, S.; Sheng, W.; Yabuuchi, N.; Kim, Y.-T.; Mitani, T.; Vescovo, E.; Shao-Horn, Y. Roles of Surface Steps on Pt Nanoparticles in Electro-oxidation of Carbon Monoxide and Methanol. *J. Am. Chem. Soc.* 2009, *131*, 15669-15677.

113. Park, S.; Xie, Y.; Weaver, M. J. Electrocatalytic Pathways on Carbon-Supported Platinum Nanoparticles: Comparison of Particle-Size-Dependent Rates of Methanol, Formic Acid, and Formaldehyde Electrooxidation. *Langmuir* 2002, *18*, 5792-5798.

114. Neurock, M.; Janik, M.; Wieckowski, A. A first principles comparison of the mechanism and site requirements for the electrocatalytic oxidation of methanol and formic acid over Pt. *Faraday Discuss.* 2009, *140*, 363-378.

115. Kristian, N.; Yan, Y.; Wang, X. Highly efficient submonolayer Pt-decorated Au nano-catalysts for formic acid oxidation. *Chem. Commun.* 2008, 353-355.

116. Anderson, R. M.; Yancey, D. F.; Loussaert, J. A.; Crooks, R. M. Multistep Galvanic Exchange Synthesis Yielding Fully Reduced Pt Dendrimer-Encapsulated Nanoparticles. *Langmuir* 2014, *30*, 15009-15015.

117. Loukrakpam, R.; Yuan, Q.; Petkov, V.; Gan, L.; Rudi, S.; Yang, R.; Huang, Y.; Brankovic, S. R.; Strasser, P. Efficient C-C bond splitting on Pt monolayer and sub-monolayer catalysts during ethanol electro-oxidation: Pt layer strain and morphology effects. *Phys. Chem. Chem. Phys.* 2014, *16*, 18866-18876.

118. Ortiz, R.; Cuesta, A.; Márquez, O. P.; Márquez, J.; Méndez, J. A.; Gutiérrez, C. Origin of the infrared reflectance increase produced by the adsorption of CO on particulate metals deposited on moderately reflecting substrates. *J. Electroanal. Chem.* 1999, *465*, 234-238.

119. Lu, G.-Q.; Sun, S.-G.; Chen, S.-P.; Cai, L.-R. Novel properties of dispersed Pt and Pd thin layers supported on GC for CO adsorption studied using in situ MS-FTIR

reflection spectroscopy. *J. Electroanal. Chem.* 1997, *421*, 19-23.

120. Porezag, D.; Pederson, M. R. Infrared intensities and Raman-scattering activities within density-functional theory. *Phys. Rev. B* 1996, *54*, 7830-7836.

121. Monkhorst, H. J.; Pack, J. D. Special points for Brillouin-zone integrations. *Phys. Rev. B* 1976, *13*, 5188-5192.

122. Brankovic, S. R.; Wang, J. X.; Adzic, R. R. Metal monolayer deposition by replacement of metal adlayers on electrode surfaces. *Surf. Sci.* 2001, *474*, L173-L179.

123. Brankovic, S. R.; Wang, J. X.; Adžić, R. R. Pt Submonolayers on Ru Nanoparticles: A Novel Low Pt Loading, High CO Tolerance Fuel Cell Electrocatalyst. *Electrochem. Solid-State Lett.* 2001, *4*, A217-A220.

124. Maillard, F.; Savinova, E. R.; Simonov, P. A.; Zaikovskii, V. I.; Stimming, U. Infrared Spectroscopic Study of CO Adsorption and Electro-oxidation on Carbon-Supported Pt Nanoparticles: Interparticle versus Intraparticle Heterogeneity. *J. Phys. Chem. B* 2004, *108*, 17893-17904.

125. Albiter, M. A.; Crooks, R. M.; Zaera, F. Adsorption of Carbon Monoxide on Dendrimer-Encapsulated Platinum

Nanoparticles: Liquid versus Gas Phase. *J. Phys. Chem. Lett.* 2009, *1*, 38-40.

126. Marković, N. M.; Lucas, C. A.; Rodes, A.; Stamenković, V.; Ross, P. N. Surface electrochemistry of CO on Pt(1 1 1): anion effects. *Surf. Sci.* 2002, *499*, L149-L158.

127. Villegas, I.; Weaver, M. J. Carbon monoxide adlayer structures on platinum (111) electrodes: A synergy between in-situ scanning tunneling microscopy and infrared spectroscopy. *J. Chem. Phys.* 1994, *101*, 1648-1660.

128. López-Cudero, A.; Cuesta, A.; Gutiérrez, C. Potential dependence of the saturation CO coverage of Pt electrodes: The origin of the pre-peak in CO-stripping voltammograms. Part 1: Pt(1 1 1). *J. Electroanal. Chem.* 2005, *579*, 1-12.